



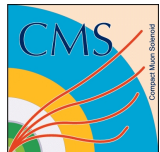
Universiteit Gent
Faculteit Wetenschappen
Vakgroep Fysica en Sterrenkunde

² No title yet

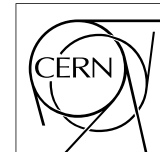
³ No sub-title neither, obviously...

⁴ Alexis Fagot

⁵



Thesis to obtain the degree of
Doctor of Philosophy in Physics
Academic years 2012-2017



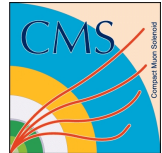


Universiteit Gent
Faculteit Wetenschappen
Vakgroep Fysica en Sterrenkunde

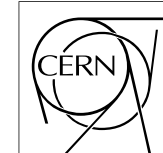
Promotoren: Dr. Michael Tytgat
Prof. Dr. Dirk Ryckbosch

Universiteit Gent
Faculteit Wetenschappen
Vakgroep Fysica en Sterrenkunde
Proeftuinstraat 86, B-9000 Gent, België
Tel.: +32 9 264.65.28
Fax.: +32 9 264.66.97

17



Thesis to obtain the degree of
Doctor of Philosophy in Physics
Academic years 2012-2017



18

Acknowledgements

19 Ici on remerciera tous les gens que j'ai pu croiser durant cette aventure et qui m'ont
20 permis de passer un bon moment

21

Gent, ici la super date de la mort qui tue de la fin d'écriture

22

Alexis Fagot

Table of Contents

23

24	Acknowledgements	i
25	Nederlandse samenvatting	xix
26	English summary	xxi
27	1 Introduction	1-1
28	1.1 A story of High Energy Physics	1-1
29	1.2 Organisation of this study	1-1
30	2 Investigating the TeV scale	2-1
31	2.1 The Standard Model of Particle Physics	2-1
32	2.2 The Large Hadron Collider and the Compact Muon Solenoid	2-1
33	2.3 Muon Phase-II Upgrade	2-1
34	3 Amplification processes in gaseous detectors	3-1
35	3.1 Signal formation	3-1
36	3.2 Gas transport parameters	3-1
37	4 Resistive Plate Chambers	4-1
38	4.1 Principle	4-1
39	4.2 Rate capability of Resistive Plate Chambers	4-1
40	4.3 High time resolution	4-1
41	4.4 Resistive Plate Chambers at CMS	4-1
42	4.4.1 Overview	4-1
43	4.4.2 The present RPC system	4-2
44	4.4.3 Pulse processing of CMS RPCs	4-3
45	5 Longevity studies and Consolidation of the present CMS RPC subsystem	5-1
46	5.1 Testing detectors under extreme conditions	5-1
47	5.1.1 The Gamma Irradiation Facilities	5-3
48	5.1.1.1 GIF	5-3
49	5.1.1.2 GIF++	5-5
50	5.2 Preliminary tests at GIF	5-8
51	5.2.1 Resistive Plate Chamber test setup	5-8

53	5.2.2	Data Acquisition	5-10
54	5.2.3	Geometrical acceptance of the setup layout to cosmic muons	5-10
55	5.2.3.1	Description of the simulation layout	5-11
56	5.2.3.2	Simulation procedure	5-13
57	5.2.3.3	Results	5-14
58	5.2.4	Photon flux at GIF	5-15
59	5.2.4.1	Expectations from simulations	5-15
60	5.2.4.2	Dose measurements	5-19
61	5.2.5	Results and discussions	5-20
62	5.3	Longevity tests at GIF++	5-21
63	5.3.1	Description of the Data Acquisition	5-25
64	5.3.2	RPC current, environmental and operation parameter mon- itoring	5-26
65	5.3.3	Measurement procedure	5-27
66	5.3.4	Longevity studies results	5-27
67	6	Investigation on high rate RPCs	6-1
68	6.1	Rate limitations and ageing of RPCs	6-1
69	6.1.1	Low resistivity electrodes	6-1
70	6.1.2	Low noise front-end electronics	6-1
71	6.2	Construction of prototypes	6-1
72	6.3	Results and discussions	6-1
73	7	Conclusions and outlooks	7-1
74	7.1	Conclusions	7-1
75	7.2	Outlooks	7-1
76	A	A data acquisition software for CAEN VME TDCs	A-1
77	A.1	GIF++ DAQ file tree	A-1
78	A.2	Description of the readout setup	A-2
79	A.3	Data read-out	A-3
80	A.3.1	V1190A TDCs	A-4
81	A.3.2	DataReader	A-6
82	A.4	Communications	A-11
83	A.4.1	V1718 USB Bridge	A-11
84	A.4.2	Configuration file	A-12
85	A.4.3	WebDCS/DAQ intercommunication	A-14
86	A.4.4	Example of inter-process communication cycle	A-15
87	A.5	DAQ algorithm overview	A-15
88	A.6	Software export	A-15
89	B	Details on the online analysis package	B-1
90	B.1	Introduction	B-1

92	C Structure of the hybrid simulation software	C-1
93	C.1 Introduction	C-1

List of Figures

94

95	2.1	Absorbed dose in the CMS cavern after an integrated luminosity of 3000 fb. R is the transverse distance from the beamline and Z is the distance along the beamline from the Interaction Point at Z=0.	2-2
96			
97			
98	2.2	A quadrant of the muon system, showing DTs (yellow), RPCs (light blue), and CSCs (green). The locations of new forward muon detectors for Phase-II are contained within the dashed box and indicated in red for GEM stations (ME0, GE1/1, and GE2/1) and dark blue for improved RPC (iRPC) stations (RE3/1 and RE4/1).	2-3
99			
100			
101			
102			
103	2.3	RMS of the multiple scattering displacement as a function of muon p_T for the proposed forward muon stations. All of the electromag- netic processes such as bremsstrahlung and magnetic field effect are included in the simulation.	2-4
104			
105			
106			
107	4.1	Signals from the RPC strips are shaped by the FEE described on Figure 4.1a. Output LVDS signals are then read-out by a TDC module connected to a computer or converted into NIM and sent to scalers. Figure 4.1b describes how these converted signals are put in coincidence with the trigger.	4-4
108			
109			
110			
111			
112	4.2	Description of the principle of a CFD. A comparison of threshold triggering (left) and constant fraction triggering (right) is shown in Figure 4.2a. Constant fraction triggering is obtained thanks to zero-crossing technique as explained in Figure 4.2b. The signal arriving at the input of the CFD is split into three components. A first one is delayed and connected to the inverting input of a first comparator. A second component is connected to the noninverting input of this first comparator. A third component is connected to the noninverting input of another comparator along with a thresh- old value connected to the inverting input. Finally, the output of both comparators is fed through an AND gate.	4-5
113			
114			
115			
116			
117			
118			
119			
120			
121			
122			
123	5.1	(5.1a) Extrapolation from 2016 data of single hit rate per unit area in the barrel region. (5.1b) Extrapolation from 2016 data of single hit rate per unit area in the endcap region.	5-2
124			
125			

126	5.2	Background Fluka simulation compared to 2016 Data at $L = 10^{34} \text{ cm}^{-2} \cdot \text{s}^{-1}$ in the fourth endcap disk region. A mismatch in between simulation and data can be observed. [To be understood.]	5-3
129	5.3	Layout of the test beam zone called X5c GIF at CERN. Photons from the radioactive source produce a sustained high rate of random hits over the whole area. The zone is surrounded by 8 m high and 80 cm thick concrete walls. Access is possible through three entry points. Two access doors for personnel and one large gate for material. A crane allows installation of heavy equipment in the area.	5-4
136	5.4	^{137}Cs decays by β^- emission to the ground state of ^{137}Ba (BR = 5.64%) and via the 662 keV isomeric level of ^{137}Ba (BR = 94.36%) whose half-life is 2.55 min.	5-5
139	5.5	Floor plan of the GIF++ facility. When the facility downstream of the GIF++ takes electron beam, a beam pipe is installed along the beam line (z-axis). The irradiator can be displaced laterally (its center moves from $x = 0.65$ m to 2.15 m), to increase the distance to the beam pipe.	5-6
144	5.6	Simulated unattenuated current of photons in the xz plane (Figure 5.6a) and yz plane (Figure 5.6b) through the source at $x = 0.65$ m and $y = 0$ m. With angular correction filters, the current of 662 keV photons is made uniform in xy planes.	5-7
148	5.7	Description of the RPC setup. Dimensions are given in mm. A tent containing RPCs is placed at 1720 mm from the source container. The source is situated in the center of the container. RE-4-2-BARC-161 chamber is 160 mm inside the tent. This way, the distance between the source and the chambers plan is 2060 mm. Figure 5.7a provides a side view of the setup in the xz plane while Figure 5.7b shows a top view in the yz plane.	5-8
155	5.8	RE-4-2-BARC-161 chamber is inside the tent as described in Figure 5.7. In the top right, the two scintillators used as trigger can be seen. This trigger system has an inclination of 10° relative to horizontal and is placed above half-partition B2 of the RPCs. PMT electronics are shielded thanks to lead blocks placed in order to protect them without stopping photons from going through the scintillators and the chamber.	5-9

162	5.9 Hit distributions over all 3 partitions of RE-4-2-BARC-161 chamber is showed on these plots. Top, middle and bottom figures respectively correspond to partitions A, B, and C. These plots show that some events still occur in other half-partitions than B2, which corresponds to strips 49 to 64, in front of which the trigger is placed, contributing to the inefficiency of detection of cosmic muons.	5-10
172	5.10 Results are derived from data taken on half-partition B2 only. On the 18 th of June 2014, data has been taken on chamber RE-2-BARC-161 at building 904 (Prevessin Site) with cosmic muons providing us a reference efficiency plateau of $(97.54 \pm 0.15)\%$ represented by a black curve. A similar measurement has been done at GIF on the 21 st of July with the same chamber giving a plateau of $(78.52 \pm 0.94)\%$ represented by a red curve.	5-11
179	5.11 Representation of the layout used for the simulations of the test setup. The RPC is represented as a yellow trapezoid while the two scintillators as blue cuboids looking at the sky. A green plane corresponds to the muon generation plane within the simulation. Figure 5.7a shows a global view of the simulated setup. Figure 5.7b shows a zommed view that allows to see the 2 scintillators as well as the full RPC plane.	5-12
186	5.12 γ flux $F(D)$ is plot using values from table 5.1. As expected, the plot shows similar attenuation behaviours with increasing distance for each absorption factors.	5-15
189	5.13 Figure 5.13a shows the linear approximation fit done via formulae 5.7 on data from table 5.2. Figure 5.13b shows a comparison of this model with the simulated flux using a and b given in figure 5.13a in formulae 5.4 and the reference value $D_0 = 50\text{cm}$ and the associated flux for each absorption factor F_0^{ABS} from table 5.1	5-17
195	5.14 Dose measurements has been done in a plane corresponding to the tents front side. This plan is 1900 mm away from the source. As explained in the first chapter, a lens-shaped lead filter provides a uniform photon flux in the vertical plan orthogonal to the beam direction. If the second line of measured fluxes is not taken into account because of lower values due to experimental equipments in the way between the source and the tent, the uniformity of the flux is well showed by the results.	5-19
203	5.15	5-20

204	5.16 Evolution of the maximum efficiency for RE2 (5.16a) and RE4	
205	(5.16b) chambers with increasing extrapolated γ rate per unit area	
206	at working point. Both irradiated (blue) and non irradiated (red)	
207	chambers are shown.	5-22
208	5.17 Evolution of the working point for RE2 (5.17a) and RE4 (5.17b)	
209	with increasing extrapolated γ rate per unit area at working point.	
210	Both irradiated (blue) and non irradiated (red) chambers are shown. 5-23	
211	5.18 Evolution of the maximum efficiency at HL-LHC conditions, i.e.	
212	a background hit rate per unit area of 300 Hz/cm ² , with increasing	
213	integrated charge for RE2 (5.18a) and RE4 (5.18b) detectors. Both	
214	irradiated (blue) and non irradiated (red) chambers are shown. The	
215	integrated charge for non irradiated detectors is recorded during	
216	test beam periods and stays small with respect to the charge accu-	
217	mulated in irradiated chambers.	5-23
218	5.19 Comparison of the efficiency sigmoid before (triangles) and after	
219	(circles) irradiation for RE2 (5.19a) and RE4 (5.19b) detectors.	
220	Both irradiated (blue) and non irradiated (red) chambers are shown. 5-24	
221	5.20 Evolution of the Bakelite resistivity for RE2 (5.20a) and RE4 (5.20b)	
222	detectors. Both irradiated (blue) and non irradiated (red) chambers	
223	are shown.	5-24
224	5.21 Evolution of the noise rate per unit area for the irradiated chamber	
225	RE2-2-BARC-9 only.	5-25
226	A.1 (A.1a) View of the front panel of a V1190A TDC module [10].	
227	(A.1b) View of the front panel of a V1718 Bridge module [11].	
228	(A.1c) View of the front panel of a 6U 6021 VME crate [12]. . . A-3	
229	A.2 Module V1190A <i>Trigger Matching Mode</i> timing diagram [10]. . . A-4	
230	A.3 Structure of the ROOT output file generated by the DAQ. The 5	
231	branches (<code>EventNumber</code> , <code>number_of_hits</code> , <code>Quality_flag</code> , <code>TDC_channel</code>	
232	and <code>TDC_TimeStamp</code>) are visible on the left panel of the ROOT	
233	browser. On the right panel is visible the histogram corresponding	
234	to the variable <code>nHits</code> . In this specific example, there were approxi-	
235	mately 50k events recorded to measure the gamma irradiation rate	
236	on the detectors. Each event is stored as a single entry in the <code>TTree</code> . A-11	
237	A.4 WebDCS DAQ scan page. On this page, shifters need to choose	
238	the type of scan (Rate, Efficiency or Noise Reference scan), the	
239	gamma source configuration at the moment of data taking, the	
240	beam configuration, and the trigger mode. These information will	
241	be stored in the DAQ ROOT output. Are also given the minimal	
242	measurement time and waiting time after ramping up of the detec-	
243	tors is over before starting the data acquisition. Then, the list of	
244	HV points to scan and the number of triggers for each run of the	
245	scan are given in the table underneath.	A-13

List of Tables

247	5.1	Total photon flux ($E\gamma \leq 662$ keV) with statistical error predicted considering a ^{137}Cs activity of 740 GBq at different values of the distance D to the source along the x-axis of irradiation field [6]. . .	5-15
248	5.2	Correction factor c is computed thanks to formulae 5.5 taking as reference $D_0 = 50$ cm and the associated flux F_0^{ABS} for each ab- sorption factor available in table 5.1.	5-16
249	5.3	The data at D_0 in 1997 is taken from [6]. In a second step, using Equations 5.8 and 5.9, the flux at D can be estimated in 1997. Then, taking into account the attenuation of the source activity, the flux at D can be estimated at the time of the tests in GIF in 2014. Finally, assuming a sensitivity of the RPC to γ $s = 2 \cdot 10^{-3}$, an estimation of the hit rate per unit area is obtained.	5-18
250	A.1	Inter-process communication cycles in between the webDCS and the DAQ through file string signals.	A-16
251			
252			
253			
254			
255			
256			
257			
258			
259			
260			

261

List of Acronyms

262

List of Acronyms

263

264

A

265

266

267 AFL

Almost Full Level

268

269

B

270

271

272 BARC

Bhabha Atomic Research Centre

273 BLT

Block Transfer

274 BR

Branching Ratio

275

276

C

277

278

279 CAEN

Costruzioni Apparecchiature Elettroniche Nucleari S.p.A.

280

281 CERN

European Organization for Nuclear Research

282 CFD

Constant Fraction Discriminator

283 CMS

Compact Muon Solenoid

284 CSC

Cathode Strip Chamber

285

286

D

287

288

289 DAQ

Data Acquisition

290 DCS

Detector Control Software

291 DQM

Data Quality Monitoring

292	DT	Drift Tube
293		
294		
295	F	
296		
297	FEE	Front-End Electronics
298	FEB	Front-End Board
299		
300		
301	G	
302		
303	GE-/-	Find a good description
304	GE1/1	Find a good description
305	GE2/1	Find a good description
306	GEANT	GEometry ANd Tracking - a series of software toolkit platforms developed by CERN
307		
308	GEM	Gas Electron Multiplier
309	GIF	Gamma Irradiation Facility
310	GIF++	new Gamma Irradiation Facility
311		
312		
313	H	
314		
315	HL-LHC	High Luminosity LHC
316	HV	High Voltage
317		
318		
319	I	
320		
321	iRPC	improved RPC
322	IRQ	Interrupt Request
323		
324		
325	L	
326		
327	LHC	Large Hadron Collider
328	LS1	First Long Shutdown
329	LS3	Third Long Shutdown

330	LV	Low Voltage
331	LVDS	Low-Voltage Differential Signaling
332		
333		
334	M	
335		
336	MC	Monte Carlo
337	MCNP	Monte Carlo N-Particle
338	ME-/-	Find good description
339	ME0	Find good description
340		
341		
342	N	
343		
344	NIM	Nuclear Instrumentation Module logic signals
345		
346		
347	P	
348		
349	PMT	PhotoMultiplier Tube
350		
351		
352	R	
353		
354	RE-/-	Find a good description
355	RE2/2	Find a good description
356	RE3/1	Find a good description
357	RE3/2	Find a good description
358	RE4/1	Find a good description
359	RE4/2	Find a good description
360	RE4/3	Find a good description
361	RMS	Root Mean Square
362	ROOT	a framework for data processing born at CERN
363	RPC	Resistive Plate Chamber
364		
365		
366	S	
367		
368	SPS	Super Proton Synchrotron

369

370

371 **T**

372

373 TDC

Time-to-Digital Converter

374

375

376 **W**

377

378 webDCS

Web Detector Control System

380

Nederlandse samenvatting –Summary in Dutch–

382 Le resume en Neerlandais (j'aurais peut-etre de apprendre la langue juste pour
383 ca...).

English summary

385 Le meme résume mais en Anglais (on commencera par la hein!).

1

Introduction

386

387

388 **1.1 A story of High Energy Physics**

389 **1.2 Organisation of this study**

2

390

391

Investigating the TeV scale

392 2.1 The Standard Model of Particle Physics

393 2.2 The Large Hadron Collider and the Compact 394 Muon Solenoid

395 2.3 Muon Phase-II Upgrade

396 After the more than two years lasting First Long Shutdown (LS1), the Large
397 Hadron Collider (LHC) delivered its very first Run-II proton-proton collisions
398 early 2015. LS1 gave the opportunity to the LHC and to its experiments to
399 undergo upgrades. The accelerator is now providing collisions at center-of-mass
400 energy of 13 TeV and bunch crossing rate of 40 MHz, with a peak luminosity ex-
401 ceeding its design value. During the first and upcoming second LHC Long Shut-
402 down, the Compact Muon Solenoid (CMS) detector is also undergoing a number
403 of upgrades to maintain a high system performance [1].

404 From the LHC Phase-II or High Luminosity LHC (HL-LHC) period onwards,
405 i.e. past the Third Long Shutdown (LS3), the performance degradation due to
406 integrated radiation as well as the average number of inelastic collisions per bunch
407 crossing, or pileup, will rise substantially and become a major challenge for the
408 LHC experiments, like CMS that are forced to address an upgrade program for
409 Phase-II [2]. Simulations of the expected distribution of absorbed dose in the CMS
410 detector under HL-LHC conditions, show in figure 5.14 that detectors placed close

- ⁴¹¹ to the beamline will have to withstand high irradiation, the radiation dose being of
⁴¹² the order of a few tens of Gy.

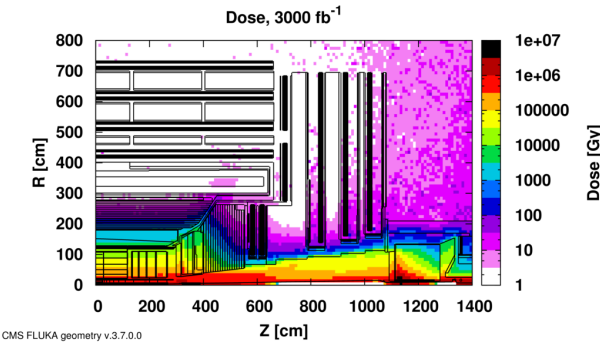


Figure 2.1: Absorbed dose in the CMS cavern after an integrated luminosity of 3000 fb. R is the transverse distance from the beamline and Z is the distance along the beamline from the Interaction Point at Z=0.

⁴¹³ The measurement of small production cross-section and/or decay branching
⁴¹⁴ ratio processes, such as the Higgs boson coupling to charge leptons or the $B_s \rightarrow$
⁴¹⁵ $\mu^+ \mu^-$ decay, is of major interest and specific upgrades in the forward regions of
⁴¹⁶ the detector will be required to maximize the physics acceptance on the largest
⁴¹⁷ possible solid angle. To ensure proper trigger performance within the present cov-
⁴¹⁸ erage, the muon system will be completed with new chambers. In figure 2.2 one
⁴¹⁹ can see that the existing Cathode Strip Chambers (CSCs) will be completed by Gas
⁴²⁰ Electron Multipliers (GEMs) and Resistive Plate Chambers (RPCs) in the pseudo-
⁴²¹ rapidity region $1.6 < |\eta| < 2.4$ to complete its redundancy as originally scheduled
⁴²² in the CMS Technical Proposal [3].

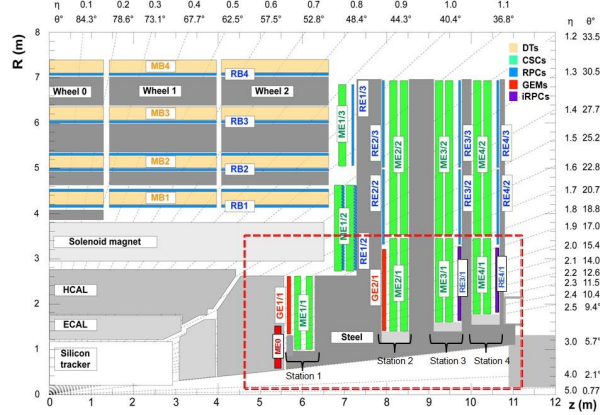


Figure 2.2: A quadrant of the muon system, showing DTs (yellow), RPCs (light blue), and CSCs (green). The locations of new forward muon detectors for Phase-II are contained within the dashed box and indicated in red for GEM stations (ME0, GE1/I, and GE2/I) and dark blue for improved RPC (iRPC) stations (RE3/1 and RE4/1).

423 RPCs are used by the CMS first level trigger for their good timing performances.
 424 Indeed, a very good bunch crossing identification can be obtained with the
 425 present CMS RPC system, given their fast response of the order of 1 ns. In order
 426 to contribute to the precision of muon momentum measurements, muon chambers
 427 should have a spatial resolution less or comparable to the contribution of multiple
 428 scattering [1]. Most of the plausible physics is covered only considering muons
 429 with $p_T < 100$ GeV thus, in order to match CMS requirements, a spatial resolu-
 430 tion of $\mathcal{O}(\text{few mm})$ the proposed new RPC stations, as shown by the simulation in
 431 figure 2.3. According to preliminary designs, RE3/1 and RE4/1 readout pitch will
 432 be comprised between 3 and 6 mm and 5 η -partitions could be considered.

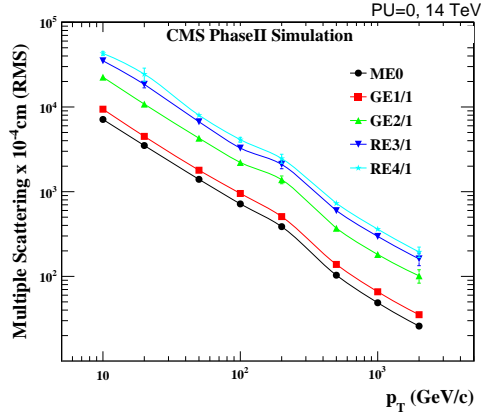


Figure 2.3: RMS of the multiple scattering displacement as a function of muon p_T for the proposed forward muon stations. All of the electromagnetic processes such as bremsstrahlung and magnetic field effect are included in the simulation.

3

433

434

435

Amplification processes in gaseous detectors

436 **3.1 Signal formation**

437 **3.2 Gas transport parameters**

4

438

439

Resistive Plate Chambers

440 4.1 Principle

441 4.2 Rate capability of Resistive Plate Chambers

442 4.3 High time resolution

443 4.4 Resistive Plate Chambers at CMS

444 4.4.1 Overview

445 The Resistive Plate Chambers (RPC) system, located in both barrel and endcap
446 regions, provides a fast, independent muon trigger with a looser p_T threshold over
447 a large portion of the pseudorapidity range ($|\eta| < 1.6$) [\[add reconstruction\]](#).

448

449 During High-Luminosity LHC (HL-LHC) operations the expected conditions
450 in terms of background and pile-up will make the identification and correct P_T as-
451 signment a challenge for the Muon system. The goal of RPC upgrade is to provide
452 additional hits to the Muon system with precise timing. All these informations will
453 be elaborated by the trigger system in a global way enhancing the performance of
454 the trigger in terms of efficiency and rate control. The RPC Upgrade is based
455 on two projects: an improved Link Board System and the extension of the RPC
456 coverage up to $|\eta| = 2.4$. [\[FIXME 2.4 or 2.5?\]](#)

457 The Link Board system, that will be described in section xxx, is responsible to
458 process, synchronize and zero-suppress the signals coming from the RPC front end
459 boards. The Link Board components have been produced between 2006 and 2007
460 and will be subjected to aging and failure in the long term. The upgraded Link
461 Board system will overcome the aging problems described in section xxx and will
462 allow for a more precise timing information to the RPC hits from 25 to 1 ns [ref
463 section xxx].

464 The extension of the RPC system up to $|\eta| = 2.1$ was already planned in the
465 CMS TDR [ref cmstdr] and staged because of budget limitations and expected
466 background rates higher than the rate capability of the present CMS RPCs in that
467 region. An extensive R&D program has been done in order to develop an improved
468 RPC that fulfills the CMS requirements. Two new RPC layers in the innermost ring
469 of stations 3 and 4 will be added with benefits to the neutron-induced background
470 reduction and efficiency improvement for both trigger and offline reconstruction.

471 4.4.2 The present RPC system

472 The RPC system is organized in 4 stations called RB1 to RB4 in the barrel region,
473 and RE1 to RE4 in the endcap region. The innermost barrel stations, RB1 and
474 RB2, are instrumented with 2 layers of RPCs facing the innermost (RB1in and
475 RB2in) and outermost (RB1out and RB2out) sides of the DT chambers. Every
476 chamber is then divided from the read-out point of view into 2 or 3 η partitions
477 called “rolls”. The RPC system consist of 480 barrel chambers and 576 endcap
478 chambers. Details on the geometry are discussed in the paper [ref to geo paper].

479 The CMS RPC chamber is a double-gap, operated in avalanche mode to ensure
480 reliable operation at high rates. Each RPC gap consists of two 2-mm-thick resistive
481 High-Pressure Laminate (HPL) plates separated by a 2-mm-thick gas gap. The
482 outer surface of the HPL plates is coated with a thin conductive graphite layer, and
483 a voltage is applied. The RPCs are operated with a 3-component, non-flammable
484 gas mixture consisting of 95.2% freon ($C_2H_2F_4$, known as R134a), 4.5% isobutane
485 ($i-C_4H_{10}$), and 0.3% sulphur hexafluoride (SF_6) with a relative humidity of 40% -
486 50%. Readout strips are aligned in η between the 2 gas gaps. [\[Add a sentence on
487 FEBs.\]](#)

488 The discriminated signals coming from the Front End boards feed via twisted
489 cables (10 to 20 m long) the Link Board System located in UXC on the balconies
490 around the detector. The Link System consist of the 1376 Link Boards (LBs)
491 and the 216 Control Boards (CBs), placed in 108 Link Boxes. The Link Box
492 is a custom crate (6U high) with 20 slots (for two CBs and eighteen LBs). The
493 Link Box contains custom backplane to which the cables from the chambers are
494 connected, as well as the cables providing the LBs and CBs power supply and the
495 cables for the RPC FEBs control with use of the I2C protocol (trough the CB). The

496 backplane itself contains only connectors (and no any other electronic devices).

497 The Link Board has 96 input channels (one channel corresponds to one RPC
498 strip). The input signals are the ~ 100 ns binary pulses which are synchronous to
499 the RPC hits, but not to the LHC clock (which drives the entire CMS electronics).
500 Thus the first step of the FEB signals processing is synchronization, i.e. assign-
501 ment of the signals to the BXes (25 ns periods). Then the data are compressed with
502 a simple zero-suppressing algorithm (the input channels are grouped into 8 bit par-
503 titions, only the partitions with at least one nonzero bit are selected for each BX).
504 Next, the non-empty partitions are time-multiplexed i.e. if there are more than one
505 such partition in a given BX, they are sent one-by-one in consecutive BXes. The
506 data from 3 neighbouring LBs are concentrated by the middle LB which contains
507 the optical transmitter for sending them to the USC over a fiber at 1.6 Gbps.

508 The Control Boards provide the communication of the control software with
509 the LBs via the FEC/CCU system. The CBs are connected into token rings, each
510 ring consists of 12 CBs of one detector tower and a FEC mezzanine board placed
511 on the CCS board located in the VME crate in the USC. In total, there are 18 rings
512 in the entire Link System. The CBs also perform automatic reloading of the LB's
513 firmware which is needed in order to avoid accumulation of the radiation induced
514 SEUs in the LBs firmware.

515 Both LBs and CB are based on the Xilinx Spartan III FPGAs, the CB addition-
516 ally contains radiation-tolerant (FLASH based) FPGA Actel ProAsicPlus.

517 The High Voltage power system is located in USC, not exposed to radiation and
518 easily accessible for any reparation. A single HV channel powers 2 RPC chambers
519 both in the barrel and endcap regions. The Low Voltage boards are located in UXC
520 on the balconies and provide the voltage to the front end electronics.

521 **4.4.3 Pulse processing of CMS RPCs**

522 Signals induced by cosmic particle in the RPC strips are shaped by standard CMS
523 RPC Front-End Electronics (FEE) following the scheme of Figure 4.1. On a first
524 stage, analogic signals are amplified and then sent to the Constant Fraction Dis-
525 criminator (CFD) described in Figure 4.2. At the end of the chain, 100 ns long
526 pulses are sent in the LVDS output. These output signal are sent on one side to a
527 V1190A Time-to-Digital Converter (TDC) module from CAEN and on the other
528 to an OR module to count the number of detected signals. Trigger and hit coïnci-
529 dences are monitored using scalers. The TDC is used to store the data into ROOT
530 files. These files are thus analysed to understand the detectors performance.

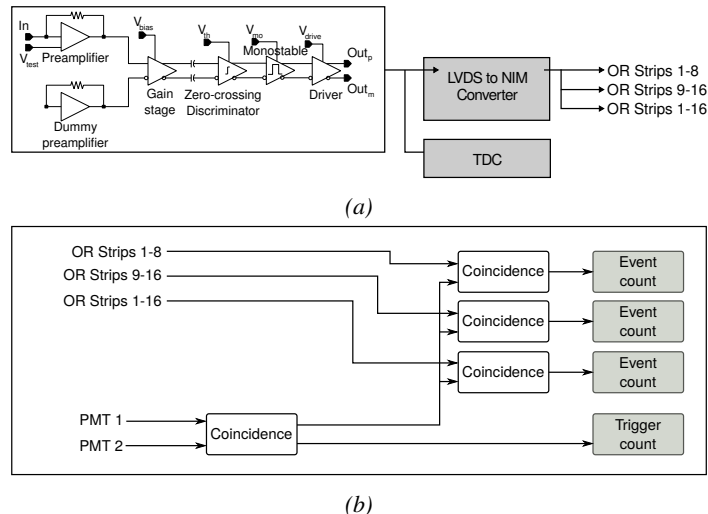


Figure 4.1: Signals from the RPC strips are shaped by the FEE described on Figure 4.1a. Output LVDS signals are then read-out by a TDC module connected to a computer or converted into NIM and sent to scalers. Figure 4.1b describes how these converted signals are put in coincidence with the trigger.

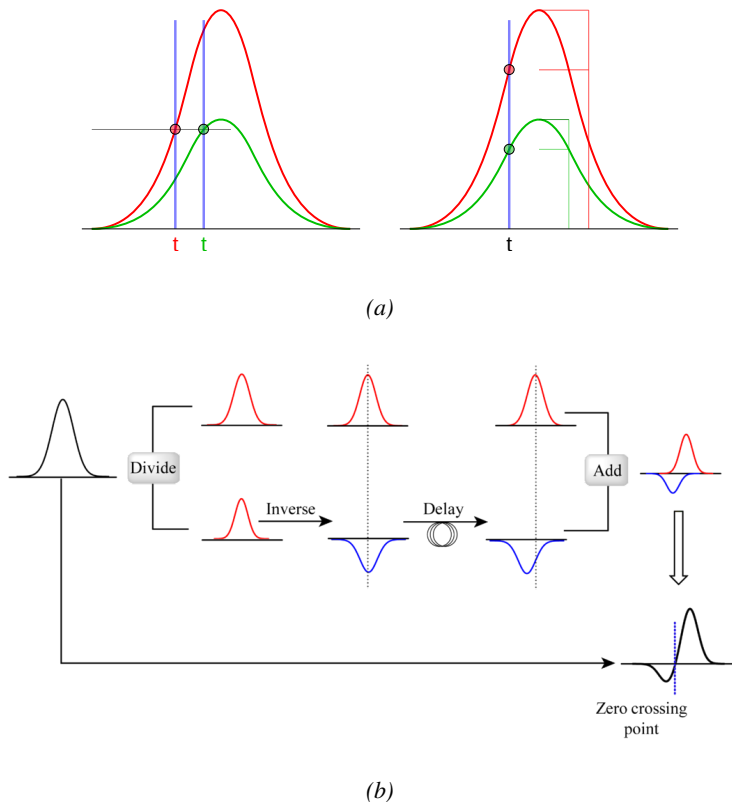


Figure 4.2: Description of the principle of a CFD. A comparison of threshold triggering (left) and constant fraction triggering (right) is shown in Figure 4.2a. Constant fraction triggering is obtained thanks to zero-crossing technique as explained in Figure 4.2b. The signal arriving at the input of the CFD is split into three components. A first one is delayed and connected to the inverting input of a first comparator. A second component is connected to the noninverting input of this first comparator. A third component is connected to the noninverting input of another comparator along with a threshold value connected to the inverting input. Finally, the output of both comparators is fed through an AND gate.

5

531

532 Longevity studies and Consolidation of 533 the present CMS RPC subsystem

534 **5.1 Testing detectors under extreme conditions**

535 The upgrade from LHC to HL-LHC will increase the peak luminosity from 10^{34}
536 $\text{cm}^{-2} \text{s}^{-1}$ to reach $5 \times 10^{34} \text{ cm}^{-2} \text{s}^{-1}$, increasing in the same way the total ex-
537 pected background to which the RPC system will be subjected to. Composed of
538 low energy gammas and neutrons from p - p collisions, low momentum primary
539 and secondary muons, puch-through hadrons from calorimeters, and particles pro-
540 duced in the interaction of the beams with collimators, the background will mostly
541 affect the regions of CMS that are the closest to the beam line, i.e. the RPC detec-
542 tors located in the endcaps. [\[To update.\]](#)

543

544 The 2016 data allowed to study the values of the background rate in all RPC
545 system. In Figure 5.1, the distribution of the chamber background hit rate per unit
546 area is shown at a luminosity of $5 \times 10^{34} \text{ cm}^{-2} \cdot \text{s}^{-1}$ linearly extrapolating from
547 data collected in 2016 [\[ref mentioning the linear dependency of rate vs lumi\]](#). The
548 maximum rate per unit area at HL-LHC conditions is expected to be of the or-
549 der of 600 Hz/cm^2 (including a safety factor 3). Nevertheless, Fluka simulations
550 have conducted in order to understand the background at HL-LHC conditions. The
551 comparison to the data has shown, in Figure 5.2, a discrepancy of a factor 2 even
552 though the order of magnitude is consistent. [\[Understand mismatch.\]](#)

553

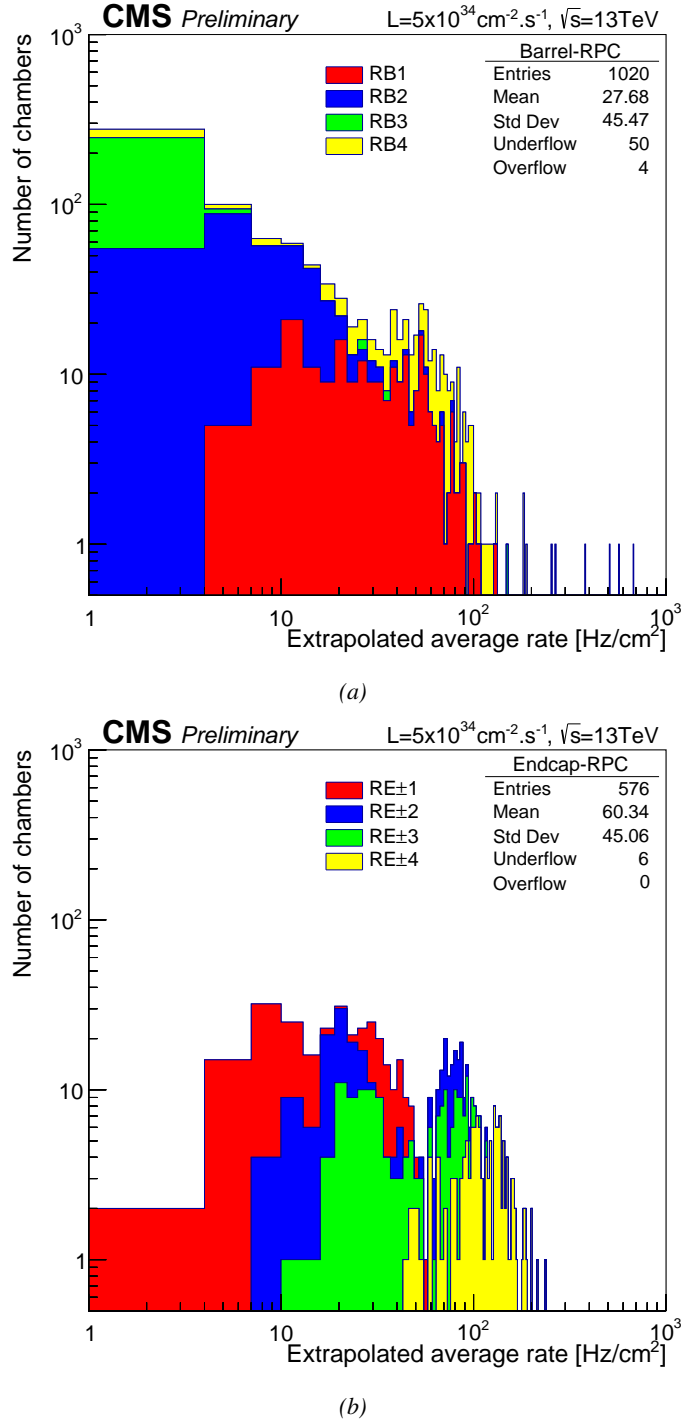


Figure 5.1: (5.1a) Extrapolation from 2016 data of single hit rate per unit area in the barrel region. (5.1b) Extrapolation from 2016 data of single hit rate per unit area in the endcap region.

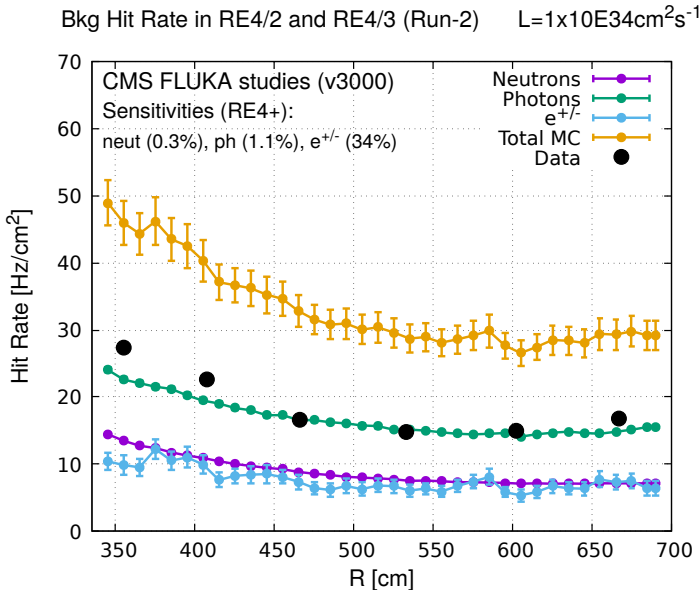


Figure 5.2: Background Fluka simulation compared to 2016 Data at $L = 10^{34} \text{ cm}^{-2} \cdot \text{s}^{-1}$ in the fourth endcap disk region. A mismatch in between simulation and data can be observed. [\[To be understood.\]](#)

554 In the past, extensive long-term tests were carried out at several gamma and
 555 neutron facilities certifying the detector performance. Both full size and small
 556 prototype RPCs have been irradiated with photons up to an integrated charge of
 557 $\sim 0.05 \text{ C}/\text{cm}^2$ and $\sim 0.4 \text{ C}/\text{cm}^2$, respectively [4, 5]. During Run-I, the RPC sys-
 558 tem provided stable operation and excellent performance and did not show any
 559 aging effects for integrated charge of the order of $0.01 \text{ C}/\text{cm}^2$. Projections on cur-
 560 rents from 2016 Data, has allowed to determine that the total integrated charge, by
 561 the end of HL-LHC, would be of the order of $1 \text{ C}/\text{cm}^2$ (including a safety factor
 562 3). [\[Corresponding figure needed.\]](#)

563

564 5.1.1 The Gamma Irradiation Facilities

565 5.1.1.1 GIF

566 Located in the SPS West Area at the downstream end of the X5 test beam, the
 567 Gamma Irradiation Facility (GIF) was a test area in which particle detectors were
 568 exposed to a particle beam in presence of an adjustable gamma background [6].
 569 Its goal was to reproduce background conditions these detectors would suffer in
 570 their operating environment at LHC. GIF layout is shown in Figure 5.3. Gamma

571 photons are produced by a strong ^{137}Cs source installed in the upstream part of the
 572 zone inside a lead container. The source container includes a collimator, designed
 573 to irradiate a $6 \times 6 \text{ m}^2$ area at 5 m maximum to the source. A thin lens-shaped lead
 574 filter helps providing with a uniform outgoing flux in a vertical plane, orthogonal
 575 to the beam direction. The principal collimator hole provides a pyramidal aperture
 576 of $74^\circ \times 74^\circ$ solid angle and provides a photon flux in a pyramidal volume along
 577 the beam axis. The photon rate is controled by further lead filters allowing the
 578 maximum rate to be limited and to vary within a range of four orders of magni-
 579 tude. Particle detectors under test are then placed within the pyramidal volume
 580 in front of the source, perpendicularly to the beam line in order to profit from the
 581 homogeneous photon flux. Adjusting the background flux of photons can then be
 582 done by using the filters and choosing the position of the detectors with respect to
 583 the source.

584

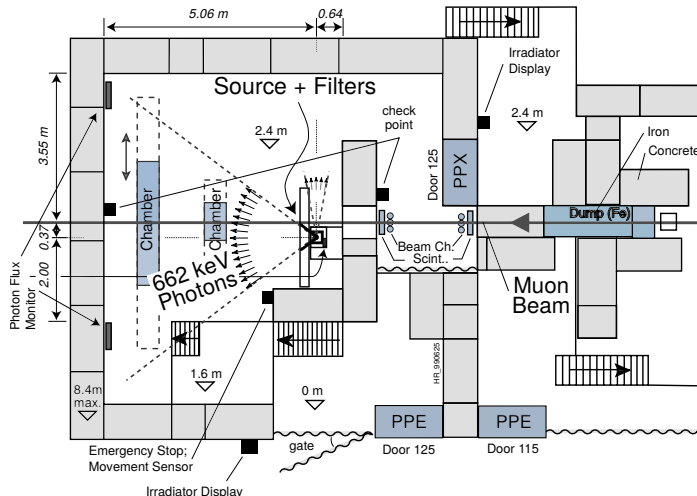


Figure 5.3: Layout of the test beam zone called X5c GIF at CERN. Photons from the radioactive source produce a sustained high rate of random hits over the whole area. The zone is surrounded by 8 m high and 80 cm thick concrete walls. Access is possible through three entry points. Two access doors for personnel and one large gate for material. A crane allows installation of heavy equipment in the area.

585 As described on Figure 5.4, the ^{137}Cs source emits a 662 keV photon in 85%
 586 of the decays. An activity of 740 GBq was measured on the 5th March 1997. To
 587 estimate the strength of the flux in 2014, it is necessary to consider the nuclear
 588 decay through time assiciated to the Cesium source whose half-life is well known
 589 ($t_{1/2} = (30.05 \pm 0.08) \text{ y}$). The GIF tests where done in between the 20th and the
 590 31st of August 2014, i.e. at a time $t = (17.47 \pm 0.02) \text{ y}$ resulting in an attenuation

591 of the activity from 740 GBq in 1997 to 494 GBq in 2014.

592

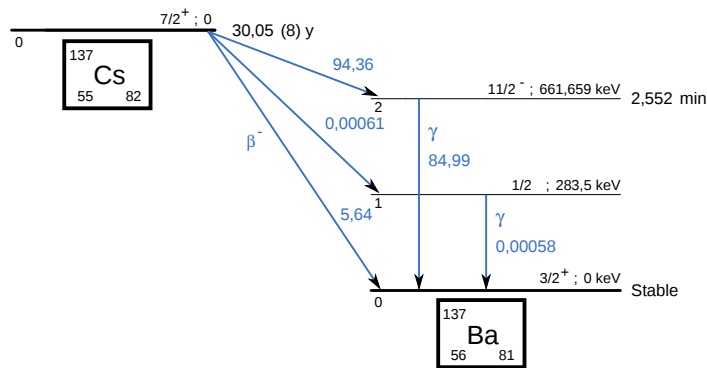


Figure 5.4: ^{137}Cs decays by β^- emission to the ground state of ^{137}Ba ($BR = 5.64\%$) and via the 662 keV isomeric level of ^{137}Ba ($BR = 94.36\%$) whose half-life is 2.55 min.

593 5.1.1.2 GIF++

594 The new Gamma Irradiation Facility (GIF++), located in the SPS North Area at
 595 the downstream end of the H4 test beam, has replaced its predecessor during LS1
 596 and has been operational since spring 2015 [7]. Like GIF, GIF++ features a ^{137}Cs
 597 source of 662 keV gamma photons, their fluence being controlled with a set of
 598 filters of various attenuation factors. The source provides two separated large irra-
 599 diation areas for testing several full-size muon detectors with continuous homo-
 600 geneous irradiation, as presented in Figure 5.5.

601

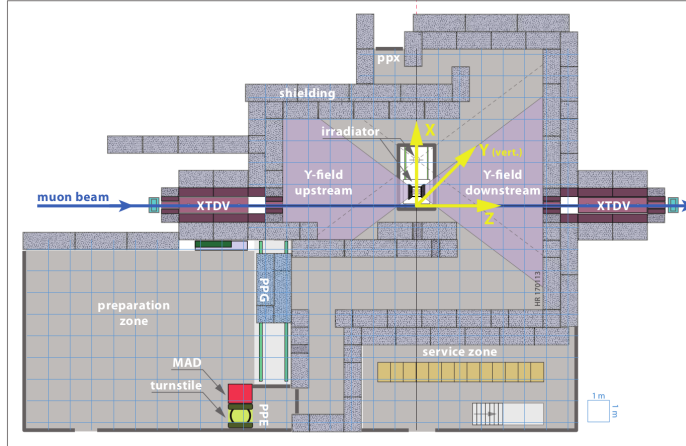


Figure 5.5: Floor plan of the GIF++ facility. When the facility downstream of the GIF++ takes electron beam, a beam pipe is installed along the beam line (z -axis). The irradiator can be displaced laterally (its center moves from $x = 0.65$ m to 2.15 m), to increase the distance to the beam pipe.

602 The source activity was measured to be about 13.5 TBq in March 2016. The
 603 photon flux being far greater than HL-LHC expectations, GIF++ provides an ex-
 604 cellent facility for accelerated aging tests of muon detectors.
 605

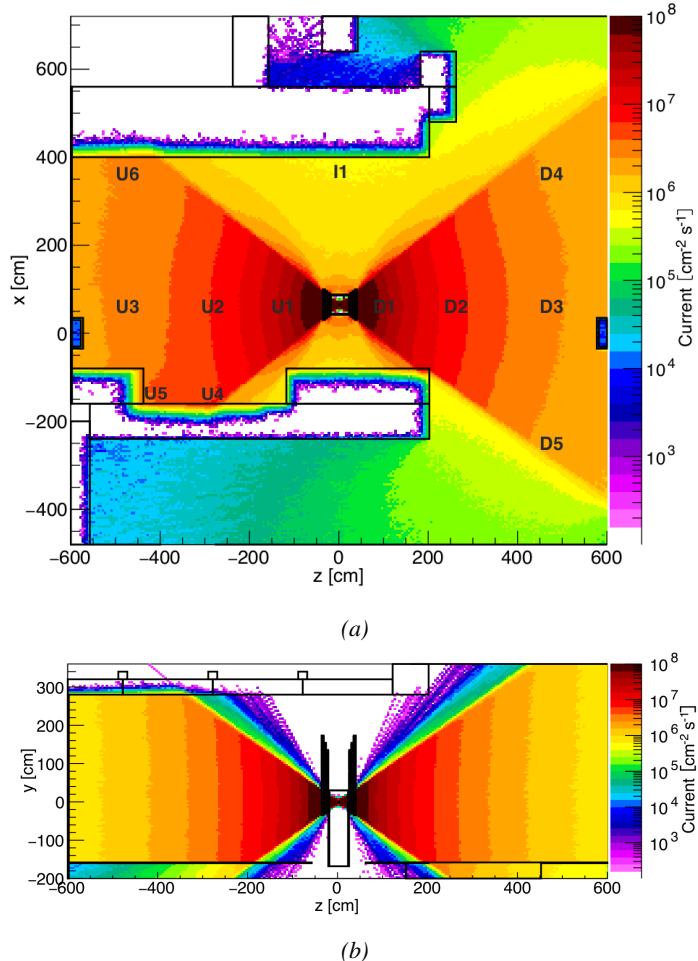


Figure 5.6: Simulated unattenuated current of photons in the xz plane (Figure 5.6a) and yz plane (Figure 5.6b) through the source at $x = 0.65$ m and $y = 0$ m. With angular correction filters, the current of 662 keV photons is made uniform in xy planes.

606 The source is situated in the muon beam line with the muon beam being avail-
 607 able a few times a year. The H4 beam, composed of muons with a momentum of
 608 about 150 GeV/c, passes through the GIF++ zone and is used to study the per-
 609 formance of the detectors. Its flux is of 104 particles/s/cm² focused in an area
 610 similar to 10×10 cm². Therefore, with properly adjusted filters, one can imitate
 611 the HL-LHC background and study the performance of muon detectors with their
 612 trigger/readout electronics in HL-LHC environment.
 613

614 5.2 Preliminary tests at GIF

615 5.2.1 Resistive Plate Chamber test setup

616 During summer 2014, preliminary tests have been conducted in the GIF area on
 617 a newly produced RE4/2 chamber labelled RE-4-2-BARC-161. This chamber has
 618 been placed into a trolley covered with a tent. The position of the RPC inside the
 619 tent and of the tent related to the source is described in Figure 5.7. To test this
 620 CMS RPC, three different absorber settings were used. First of all, measurements
 621 were done with fully opened source. Then, to complete this preliminary study,
 622 the gamma flux has been attenuated from a factor 2 and a factor 5. The expected
 623 gamma flux at the level of our detector will be discussed in subsection 5.2.4.

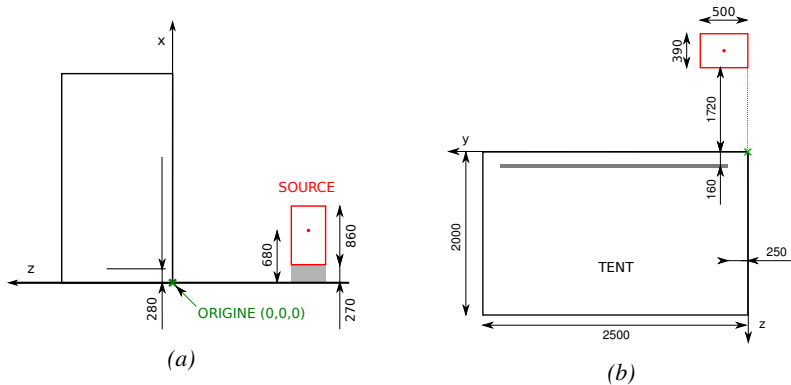


Figure 5.7: Description of the RPC setup. Dimensions are given in mm. A tent containing RPCs is placed at 1720 mm from the source container. The source is situated in the center of the container. RE-4-2-BARC-161 chamber is 160 mm inside the tent. This way, the distance between the source and the chambers plan is 2060 mm. Figure 5.7a provides a side view of the setup in the xz plane while Figure 5.7b shows a top view in the yz plane.



Figure 5.8: RE-4-2-BARC-161 chamber is inside the tent as described in Figure 5.7. In the top right, the two scintillators used as trigger can be seen. This trigger system has an inclination of 10° relative to horizontal and is placed above half-partition B2 of the RPCs. PMT electronics are shielded thanks to lead blocks placed in order to protect them without stopping photons from going through the scintillators and the chamber.

624 At the time of the tests, the beam not being operational anymore, a trigger
625 composed of 2 plastic scintillators has been placed in front of the setup with an
626 inclination of 10 deg with respect to the detector plane in order to look at cosmic
627 muons. Using this particular trigger layout, shown on Figure 5.8, leads to a cosmic
628 muon hit distribution into the chamber similar to the one in Figure 5.9. Measured
629 without gamma irradiation, two peaks can be seen on the profil of partition B, cen-
630 tered on strips 52 and 59. Section 5.2.3 will help us understand that these two peaks
631 are due respectively to forward and backward coming cosmic particles where for-
632 ward coming particles are first detected by the scintillators and then the RPC while
633 the backward coming muons are first detected in the RPC.

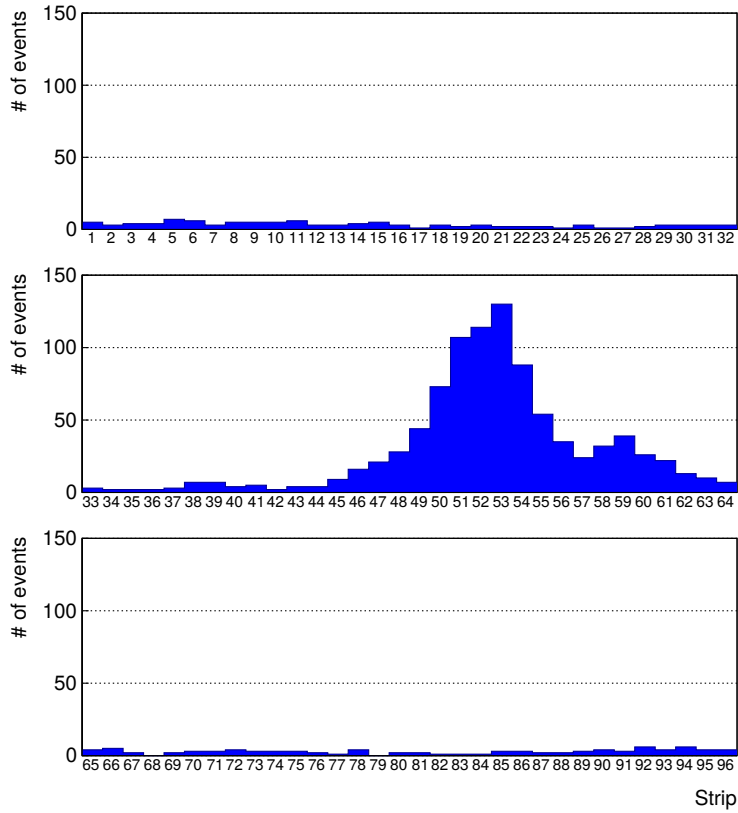


Figure 5.9: Hit distributions over all 3 partitions of RE-4-2-BARC-161 chamber is showed on these plots. Top, middle and bottom figures respectively correspond to partitions A, B, and C. These plots show that some events still occur in other half-partitions than B2, which corresponds to strips 49 to 64, in front of which the trigger is placed, contributing to the inefficiency of detection of cosmic muons. In the case of partitions A and C, the very low amount of data can be interpreted as noise. On the other hand, it is clear that a little portion of muons reach the half-partition B1, corresponding to strips 33 to 48.

634 5.2.2 Data Acquisition

635 5.2.3 Geometrical acceptance of the setup layout to cosmic muons

636 In order to profit from a constant gamma irradiation, the detectors inside of the GIF
 637 bunker need to be placed in a plane orthogonal to the beam line. The muon beam
 638 that used to be available was meant to test the performance of detectors under test.
 639 This beam not being active anymore, another solution to test detector performance
 640 had to be used. Thus, it has been decided to use cosmic muons detected through

641 a telescope composed of two scintillators. Lead blocks were used as shielding to
 642 protect the photomultipliers from gammas as can be seen from Figure 5.8.

643 An inclination has been given to the cosmic telescope to maximize the muon
 644 flux. A good compromise had to be found between good enough muon flux and
 645 narrow enough hit distribution to be sure to contain all the events into only one half
 646 partitions as required from the limited available readout hardware. Nevertheless,
 647 a consequence of the misplaced trigger, that can be seen as a loss of events in
 648 half-partition B1 in Figure 5.9, is an inefficiency. Nevertheless, the inefficiency
 649 of approximately 20 % highlighted in Figure 5.10 by comparing the performance
 650 of chamber BARC-161 in 904 and at GIF without irradiation seems too important
 651 to be explained only by the geometrical acceptance of the setup itself. Simulations
 652 have been conducted to show how the setup brings inefficiency.

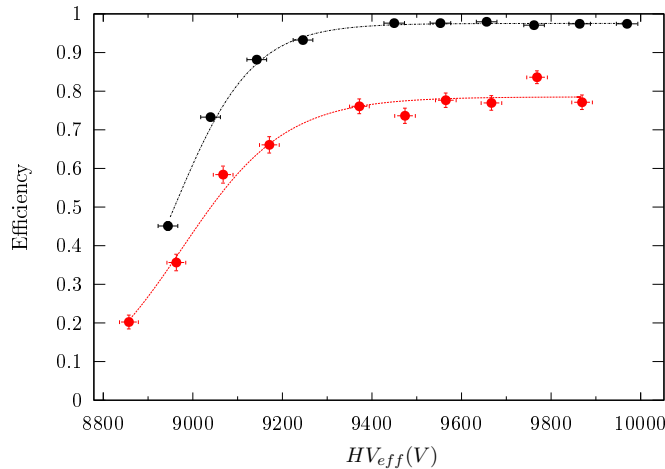


Figure 5.10: Results are derived from data taken on half-partition B2 only. On the 18th of June 2014, data has been taken on chamber RE-2-BARC-161 at building 904 (Prevessin Site) with cosmic muons providing us a reference efficiency plateau of $(97.54 \pm 0.15)\%$ represented by a black curve. A similar measurement has been done at GIF on the 21st of July with the same chamber giving a plateau of $(78.52 \pm 0.94)\%$ represented by a red curve.

653 5.2.3.1 Description of the simulation layout

654 The layout of GIF setup has been reproduced and incorporated into a Monte Carlo
 655 (MC) simulation to study the influence of the disposition of the telescope on the
 656 final distribution measured by the RPC. A 3D view of the simulated layout is given
 657 into Figure 5.11. Muons are generated randomly in a horizontal plane located at a
 658 height corresponding to the lowest point of the PMTs. This way, the needed size
 659 of the plane in order to simulate events happening at very big azimuthal angles (i.e.

660 $\theta \approx \pi$) can be kept relatively small. The muon flux is designed to follow the usual
 661 $\cos^2\theta$ distribution for cosmic particle. The goal of the simulation is to look at
 662 muons that pass through the muon telescope composed of the two scintillators and
 663 define their distribution onto the RPC plane. During the reconstruction, the RPC
 664 plane is then divided into its strips and each muon track is assigned to a strip.

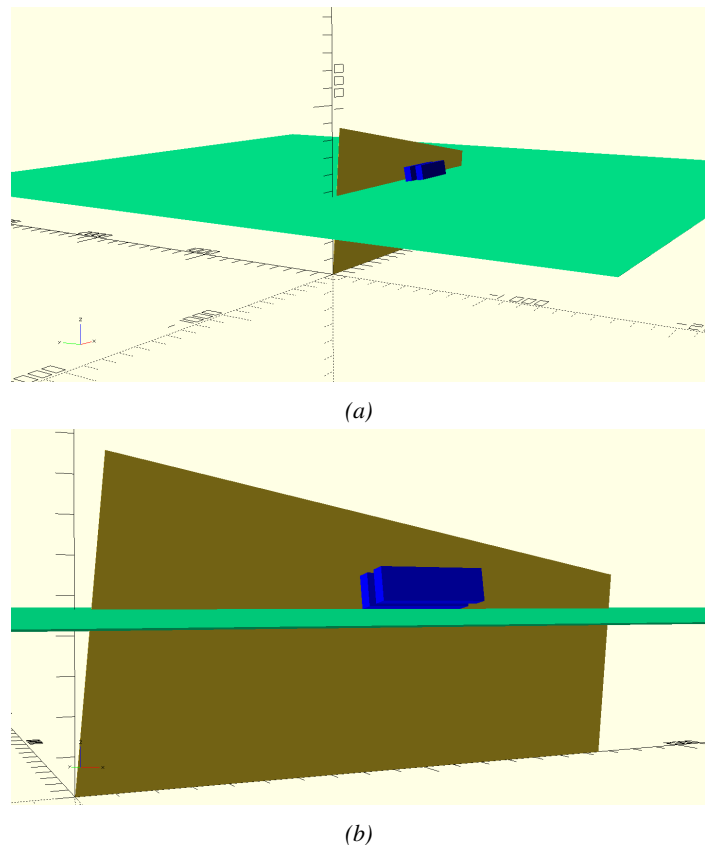


Figure 5.11: Representation of the layout used for the simulations of the test setup. The RPC is represented as a yellow trapezoid while the two scintillators as blue cuboids looking at the sky. A green plane corresponds to the muon generation plane within the simulation. Figure 5.7a shows a global view of the simulated setup. Figure 5.7b shows a zoomed view that allows to see the 2 scintillators as well as the full RPC plane.

665 In order to further refine the quality of the simulation and understand deeper
 666 the results the dependance of the distribution has been studied for a range of tele-
 667 scope inclinations. Moreover, the threshold applied on the PMT signals has been
 668 included into the simulation in the form of a cut. In the approximation of uni-
 669 form scintillators, it has been considered that the threshold can be understood as

670 the minimum distance particles need to travel through the scintillating material to
671 give a strong enough signal. Particles that travel a distance smaller than the set
672 "threshold" are thus not detected by the telescope and cannot trigger the data tak-
673 ing. Finally, the FEE threshold also has been considered in a similar way. The
674 mean momentum of horizontal cosmic rays is higher than those of vertical ones
675 but the stopping power of matter for momenta ranging from 1 GeV to 1 TeV stays
676 comparable. It is then possible to assume that the mean number of primary e^-/ion
677 pairs per unit length will stay similar and thus, depending on the applied discrimi-
678 nator threshold, muons with the shortest path through the gas volume will deposit
679 less charge and induce a smaller signal on the pick-up strips that could eventu-
680 ally not be detected. These two thresholds also restrain the overall geometrical
681 acceptance of the system.

682 **5.2.3.2 Simulation procedure**

683 The simulation software has been designed using C++ and the output data is saved
684 into ROOT histograms. Simulations start for a threshold T_{scint} varying in a range
685 from 0 to 45 mm in steps of 5 mm, where $T_{scint} = 0$ mm corresponds to the case
686 where there isn't any threshold apply on the input signal while $T_{scint} = 45$ mm,
687 which is the scintillator thickness, is the case where muons cannot arrive orthogo-
688 nally onto the scintillator surface. For a given T_{scint} , a set of RPC thresholds are
689 considered. The RPC threshold, T_{RPC} varies from 2 mm, the thickness of the gas
690 volume, to 3 mm in steps of 0.25 mm. For each $(T_{scint}; T_{RPC})$ pair, $N_\mu = 10^8$
691 muons are randomly generated inside the muon plane described in the previous
692 paragraph with an azimuthal angle θ chosen to follow a $\cos^2\theta$ distribution.

693 Planes are associated to each surface of the scintillators. Knowing muon posi-
694 tion into the muon plane and its direction allows us, by assuming that muons travel
695 in a straight line, to compute the intersection of the muon track with these planes.
696 Applying conditions to the limits of the surfaces of the scintillator faces then gives
697 us an answer to whether or not the muon passed through the scintillators. In the
698 case the muon has indeed passed through the telescope, the path through each scin-
699 tillator is computed and muons whose path was shorter than T_{scint} are rejected and
700 are thus considered as having not interacted with the setup.

701 On the contrary, if the muon is labeled as good, its position within the RPC
702 plane is computed and the corresponding strip, determined by geometrical tests
703 in the case the distance through the gas volume was enough not to be rejected
704 because of T_{RPC} , gets a hit and several histograms are filled in order to keep
705 track of the generation point on the muon plane, the intersection points of the
706 reconstructed muons within the telescope, or on the RPC plane, the path traveled
707 through each individual scintillator or the gas volume, as well as other histograms.
708 Moreover, muons fill different histograms whether they are forward or backward
709 coming muons. They are discriminated according to their direction components.

710 When a muon is generated, an (x, y, z) position is assigned into the muon plane as
 711 well as a $(\theta; \phi)$ pair that gives us the direction it's coming from. This way, muons
 712 satisfying the condition $0 \leq \phi < \pi$ are designated as backward coming muons
 713 while muons satisfying $\pi \leq \phi < 2\pi$ as forward coming muons.

714 This simulation is then repeated for different telescope inclinations ranging in
 715 between 4 and 20° and varying in steps of 2° . Due to this inclination and to the
 716 vertical position of the detector under test, the muon distribution reconstructed in
 717 the detector plane is asymmetrical. The choice has been made to chose a skew
 718 distribution formula to fit the data built as the multiplication of gaussian and sig-
 719 moidal curves together. A typical gaussian formula is given as 5.1 and has three
 720 free parameters as A_g , its amplitude, \bar{x} , its mean value and σ , its root mean square.
 721 Sigmoidal curves as given by formula 5.2 are functions converging to 0 and A_s as
 722 x diverges. The inflexion point is given as x_i and λ is proportional to the slope at
 723 $x = x_i$. In the limit where $\lambda \rightarrow \infty$, the sigmoid becomes a step function.

$$g(x) = A_g e^{\frac{-(x-\bar{x})^2}{2\sigma^2}} \quad (5.1)$$

$$s(x) = \frac{A_s}{1 + e^{-\lambda(x-x_i)}} \quad (5.2)$$

724 Finally, a possible representation of a skew distribution is given by formula 5.3
 725 and is the product of 5.1 and 5.2. Naturally, here $A_{sk} = A_g \times A_s$ and represents
 726 the theoretical maximum in the limit where the skew tends to a gaussian function.

$$sk(x) = g(x) \times s(x) = A_{sk} \frac{e^{\frac{-(x-\bar{x})^2}{2\sigma^2}}}{1 + e^{-\lambda(x-x_i)}} \quad (5.3)$$

727 5.2.3.3 Results

728 Influence of T_{scint} on the muon distribution

729 Influence of T_{RPC} on the muon distribution

730 Influence of the telescope inclination on the muon distribution

731 Comparison to data taken at GIF without irradiation

5.2.4 Photon flux at GIF

5.2.4.1 Expectations from simulations

In order to understand and evaluate the γ flux in the GIF area, simulations had been conducted in 1999 and published by S. Agosteo et al [6]. Table 5.1 presented in this article gives us the γ flux for different distances D to the source. This simulation was done using GEANT and a Monte Carlo N-Particle (MCNP) transport code, and the flux F is given in number of γ per unit area and unit time along with the estimated error from these packages expressed in %.

Nominal ABS	Photon flux F [$s^{-1}cm^{-2}$]			
	at $D = 50$ cm	at $D = 155$ cm	at $D = 300$ cm	at $D = 400$ cm
1	$0.12 \cdot 10^8 \pm 0.2\%$	$0.14 \cdot 10^7 \pm 0.5\%$	$0.45 \cdot 10^6 \pm 0.5\%$	$0.28 \cdot 10^6 \pm 0.5\%$
2	$0.68 \cdot 10^7 \pm 0.3\%$	$0.80 \cdot 10^6 \pm 0.8\%$	$0.25 \cdot 10^6 \pm 0.8\%$	$0.16 \cdot 10^6 \pm 0.6\%$
5	$0.31 \cdot 10^7 \pm 0.4\%$	$0.36 \cdot 10^6 \pm 1.2\%$	$0.11 \cdot 10^6 \pm 1.2\%$	$0.70 \cdot 10^5 \pm 0.9\%$

Table 5.1: Total photon flux ($E\gamma \leq 662$ keV) with statistical error predicted considering a ^{137}Cs activity of 740 GBq at different values of the distance D to the source along the x-axis of irradiation field [6].

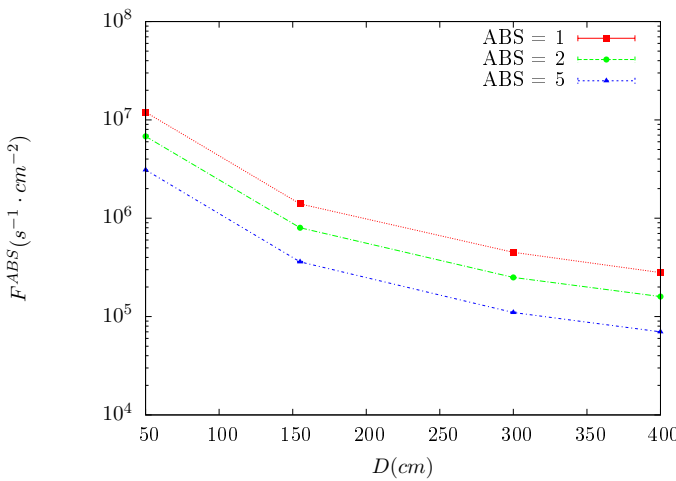


Figure 5.12: γ flux $F(D)$ is plot using values from table 5.1. As expected, the plot shows similar attenuation behaviours with increasing distance for each absorption factors.

The simulation doesn't directly provide us with an estimated flux at the level of our RPC. First of all, it is needed to extract the value of the flux from the available data contained in the original paper and then to estimate the flux in 2014 at the time the experimentation took place. Figure 5.12 that contains the data from

744 Table 5.1. In the case of a pointlike source emitting isotropic and homogeneous
 745 gamma radiations, the gamma flux F at a distance D to the source with respect
 746 to a reference point situated at D_0 where a known flux F_0 is measured will be
 747 expressed like in Equation 5.4, assuming that the flux decreases as $1/D^2$, where c
 748 is a fitting factor.

$$F^{ABS} = F_0^{ABS} \times \left(\frac{cD_0}{D} \right)^2 \quad (5.4)$$

749 By rewriting Equation 5.4, it comes that :

$$c = \frac{D}{D_0} \sqrt{\frac{F^{ABS}}{F_0^{ABS}}} \quad (5.5)$$

$$\Delta c = \frac{c}{2} \left(\frac{\Delta F^{ABS}}{F^{ABS}} + \frac{\Delta F_0^{ABS}}{F_0^{ABS}} \right) \quad (5.6)$$

750 Finally, using Equation 5.5 and the data in Table 5.1 with $D_0 = 50$ cm as
 751 reference point, we can build Table 5.2. It is interesting to note that c for each
 752 value of D doesn't depend on the absorption factor.

Nominal ABS	Correction factor c		
	at $D = 155$ cm	at $D = 300$ cm	at $D = 400$ cm
1	$1.059 \pm 0.70\%$	$1.162 \pm 0.70\%$	$1.222 \pm 0.70\%$
2	$1.063 \pm 1.10\%$	$1.150 \pm 1.10\%$	$1.227 \pm 0.90\%$
5	$1.056 \pm 1.60\%$	$1.130 \pm 1.60\%$	$1.202 \pm 1.30\%$

Table 5.2: Correction factor c is computed thanks to formulae 5.5 taking as reference $D_0 = 50$ cm and the associated flux F_0^{ABS} for each absorption factor available in table 5.1.

753 For the range of D/D_0 values available, it is possible to use a simple linear
 754 fit to get the evolution of c . The linear fit will then use only 2 free parameters, a
 755 and b , as written in Equation 5.7. This gives us the results showed in Figure 5.13.
 756 Figure 5.13b confirms that using only a linear fit to extract c is enough as the
 757 evolution of the rate that can be obtained superimposes well on the simulation
 758 points.

$$c \left(\frac{D}{D_0} \right) = a \frac{D}{D_0} + b \quad (5.7)$$

$$F^{ABS} = F_0^{ABS} \left(a + \frac{bD_0}{D} \right)^2 \quad (5.8)$$

$$\Delta F^{ABS} = F^{ABS} \left[\frac{\Delta F_0^{ABS}}{F_0^{ABS}} + 2 \frac{\Delta a + \Delta b \frac{D_0}{D}}{a + \frac{bD_0}{D}} \right] \quad (5.9)$$

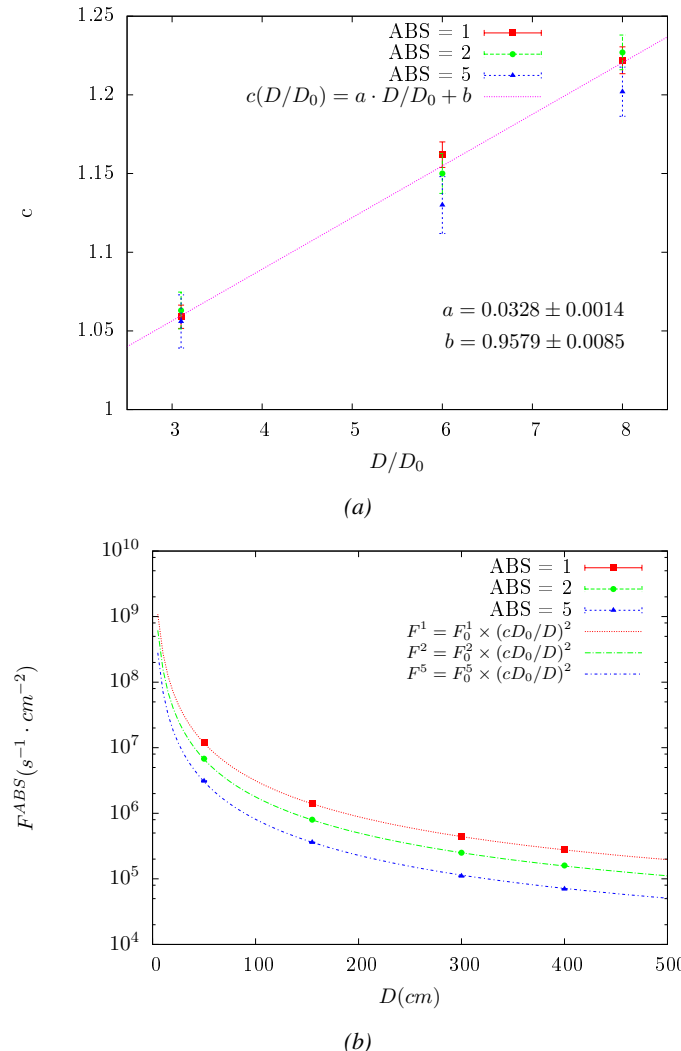


Figure 5.13: Figure 5.13a shows the linear approximation fit done via formulae 5.7 on data from table 5.2. Figure 5.13b shows a comparison of this model with the simulated flux using a and b given in figure 5.13a in formulae 5.4 and the reference value $D_0 = 50\text{cm}$ and the associated flux for each absorption factor F_0^{ABS} from table 5.1

In the case of the 2014 GIF tests, the RPC plane is located at a distance $D = 206\text{ cm}$ to the source. Moreover, to estimate the strength of the flux in 2014, it is necessary to consider the nuclear decay through time associated to the Cesium source whose half-life is well known ($t_{1/2} = (30.05 \pm 0.08)\text{y}$). The very first source activity measurement has been done on the 5th of March 1997 while the

764 GIF tests were done between the 20th and the 31st of August 2014, i.e. at a
 765 time $t = (17.47 \pm 0.02)$ y resulting in an attenuation of the activity from 740 GBq
 766 in 1997 to 494 GBq in 2014. All the needed information to extrapolate the flux
 767 through our detector in 2014 has now been assembled, leading to the Table 5.3. It
 768 is interesting to note that for a common RPC sensitivity to γ of $2 \cdot 10^{-3}$, the order
 769 of magnitude of the estimated hit rate per unit area is of the order of the kHz for
 770 the fully opened source. Moreover, taking profit of the two working absorbers, it
 771 will be possible to scan background rates at 0 Hz, ~ 300 Hz as well as ~ 600 Hz.
 772 Without source, a good estimate of the intrinsic performance will be available.
 773 Then at 300 Hz, the goal will be to show that the detectors fulfill the performance
 774 certification of CMS RPCs. Then a first idea of the performance of the detectors at
 775 higher background will be provided with absorption factors 2 (~ 600 Hz) and 1 (no
 776 absorption). *[Here I will also put a reference to the plot showing the estimated
 777 background rate at the level of RE3/I in the case of HL-LHC but this one being
 778 in another chapter, I will do it later.]*

Nominal ABS	Photon flux F [$s^{-1}cm^{-2}$]			Hit rate/unit area [$Hz cm^{-2}$] at $D^{2014} = 206$ cm
	at $D_0^{1997} = 50$ cm	at $D^{1997} = 206$ cm	at $D^{2014} = 206$ cm	
1	$0.12 \cdot 10^8 \pm 0.2\%$	$0.84 \cdot 10^6 \pm 0.3\%$	$0.56 \cdot 10^6 \pm 0.3\%$	1129 ± 32
2	$0.68 \cdot 10^7 \pm 0.3\%$	$0.48 \cdot 10^6 \pm 0.3\%$	$0.32 \cdot 10^6 \pm 0.3\%$	640 ± 19
5	$0.31 \cdot 10^7 \pm 0.4\%$	$0.22 \cdot 10^6 \pm 0.3\%$	$0.15 \cdot 10^6 \pm 0.3\%$	292 ± 9

Table 5.3: The data at D_0 in 1997 is taken from [6]. In a second step, using Equations 5.8 and 5.9, the flux at D can be estimated in 1997. Then, taking into account the attenuation of the source activity, the flux at D can be estimated at the time of the tests in GIF in 2014. Finally, assuming a sensitivity of the RPC to γ $s = 2 \cdot 10^{-3}$, an estimation of the hit rate per unit area is obtained.

779 **5.2.4.2 Dose measurements**

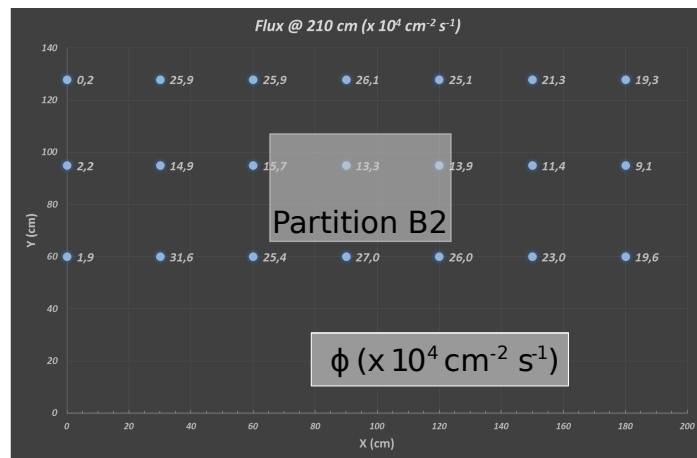


Figure 5.14: Dose measurements has been done in a plane corresponding to the tents front side. This plan is 1900 mm away from the source. As explained in the first chapter, a lens-shaped lead filter provides a uniform photon flux in the vertical plan orthogonal to the beam direction. If the second line of measured fluxes is not taken into account because of lower values due to experimental equipments in the way between the source and the tent, the uniformity of the flux is well showed by the results.

780 5.2.5 Results and discussions

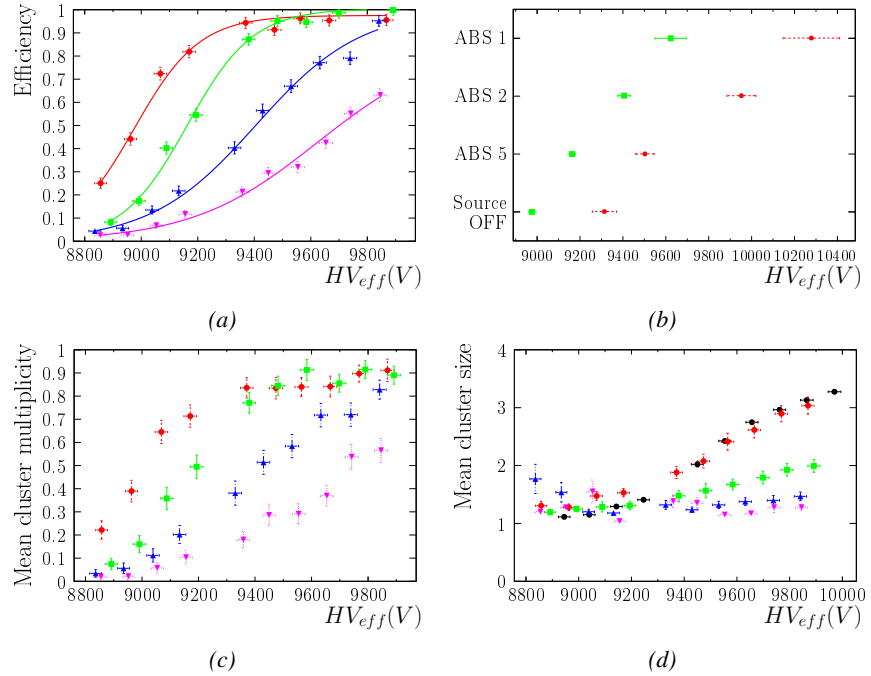


Figure 5.15

5.3 Longevity tests at GIF++

781 Longevity studies imply a monitoring of the performance of the detectors probed
782 using a high intensity muon beam in a irradiated environment by periodically mea-
783 suring their rate capability, the dark current running through them and the bulk
784 resistivity of the Bakelite composing their electrodes. GIF++, with its very intense
785 ^{137}Cs source, provides the perfect environment to perform such kind of tests. As-
786 suming a maximum acceleration factor of 3, it is expected to accumulate the equiv-
787 alent charge in 1.7 years.

788 As the maximum background is found in the endcap, the choice naturally was
789 made to focus the GIF++ longevity studies on endcap chambers. Most of the RPC
790 system was installed in 2007. Nevertheless, the large chambers in the fourth end-
791 cap (RE4/2 and RE4/3) have been installed during LS1 in 2014. The Bakelite of
792 these two different productions having different properties, four spare chambers
793 of the present system were selected, two RE2,3/2 spares and two RE4/2 spares.
794 Having two chambers of each type allows to always keep one of them non irradia-
795 ted as reference, the performance evolution of the irradiated chamber being then
796 compared through time to the performance of the non irradiated one.

797 The performance of the detectors under different level of irradiation is measured
798 periodically during dedicated test beam periods using the H4 muon beam. In be-
799 tween these test beam periods, the two RE2,3/2 and RE4/2 chambers selected for
800 this study are irradiated by the ^{137}Cs source in order to accumulate charge and
801 the gamma background is monitored, as well as the currents. The two remaining
802 chambers are kept non-irradiated as reference detectors. Due to the limited gas
803 flow in GIF++, the RE4 chamber remained non-irradiated until end of November
804 2016 where a new mass flow controller has been installed allowing for bigger vol-
805 umes of gas to flow in the system.

806 Figures 5.16 and 5.17 give us for different test beam periods, and thus for in-
807 creasing integrated charge through time, a comparison of the maximum efficiency,
808 obtained using a sigmoid-like function, and of the working point of both irradiated
809 and non irradiated chambers [8]. No aging is yet to see from this data, the shifts in
810 γ rate per unit area in between irradiated and non irradiated detectors and RE2 and
811 RE4 types being easily explained by a difference of sensitivity due to the various
812 Bakelite resistivities of the HPL electrodes used for the electrode production.

813 Collecting performance data at each test beam period allows us to extrapolate the
814 maximum efficiency for a background hit rate of 300 Hz/cm^2 corresponding to
815 the expected HL-LHC conditions. Aging effects could emerge from a loss of ef-
816 ficiency with increasing integrated charge over time, thus Figure 5.18 helps us
817 understand such degradation of the performance of irradiated detectors in compar-
818 ison with non irradiated ones. The final answer for an eventual loss of efficiency is
819 given in Figure 5.19 by comparing for both irradiated and non irradiated detectors

the efficiency sigmoids before and after the longevity study. Moreover, to complete the performance information, the Bakelite resistivity is regularly measured thanks to Ag scans (Figure 5.20) and the noise rate is monitored weekly during irradiation periods (Figure 5.21). At the end of 2016, no signs of aging were observed and further investigation is needed to get closer to the final integrated charge requirements proposed for the longevity study of the present CMS RPC sub-system.

827

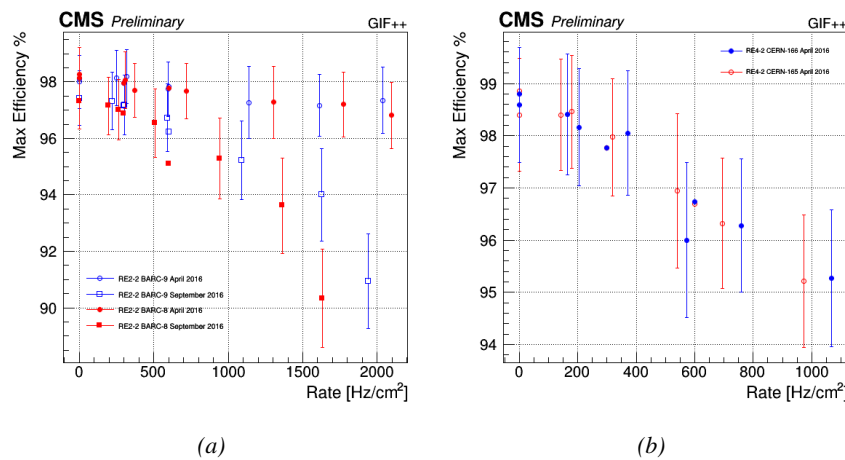


Figure 5.16: Evolution of the maximum efficiency for RE2 (5.16a) and RE4 (5.16b) chambers with increasing extrapolated γ rate per unit area at working point. Both irradiated (blue) and non irradiated (red) chambers are shown.

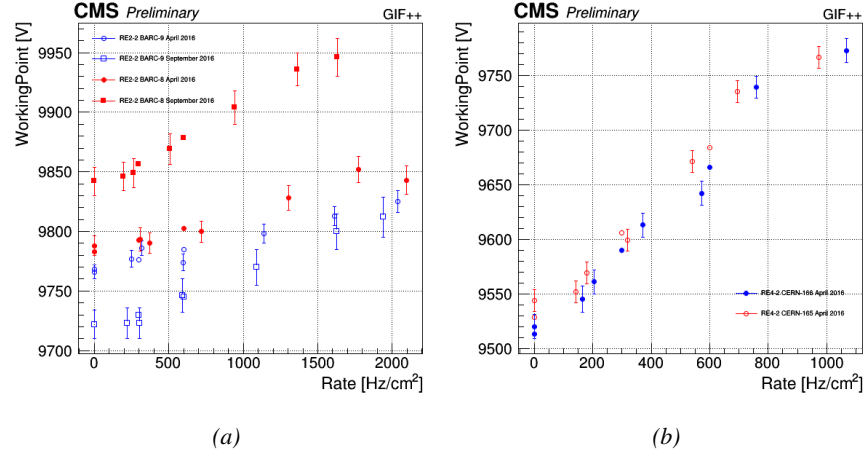


Figure 5.17: Evolution of the working point for RE2 (5.17a) and RE4 (5.17b) with increasing extrapolated γ rate per unit area at working point. Both irradiated (blue) and non irradiated (red) chambers are shown.

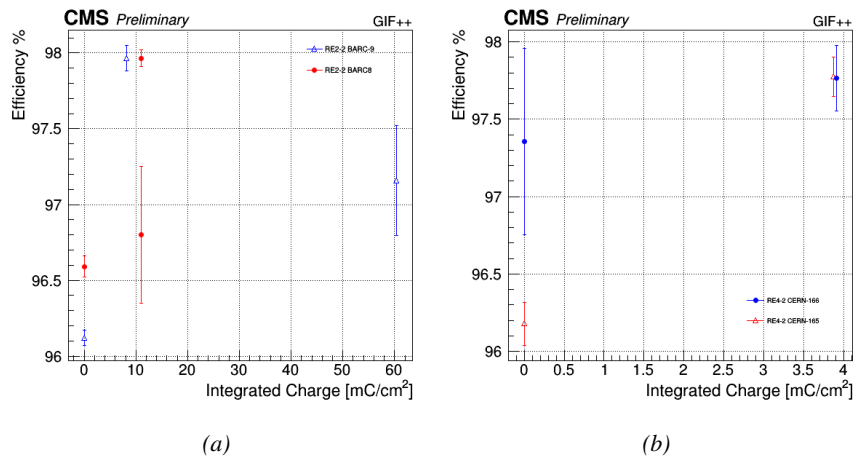


Figure 5.18: Evolution of the maximum efficiency at HL-LHC conditions, i.e. a background hit rate per unit area of 300 Hz/cm², with increasing integrated charge for RE2 (5.18a) and RE4 (5.18b) detectors. Both irradiated (blue) and non irradiated (red) chambers are shown. The integrated charge for non irradiated detectors is recorded during test beam periods and stays small with respect to the charge accumulated in irradiated chambers.

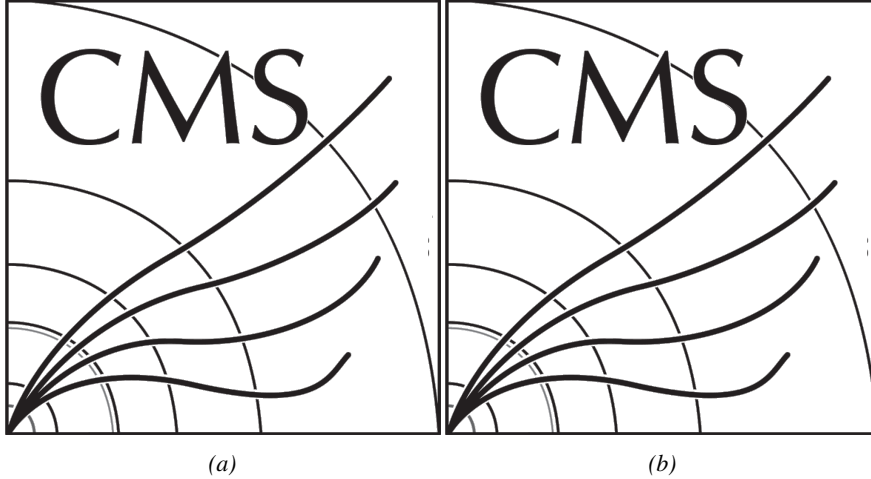


Figure 5.19: Comparison of the efficiency sigmoid before (triangles) and after (circles) irradiation for RE2 (5.19a) and RE4 (5.19b) detectors. Both irradiated (blue) and non irradiated (red) chambers are shown.

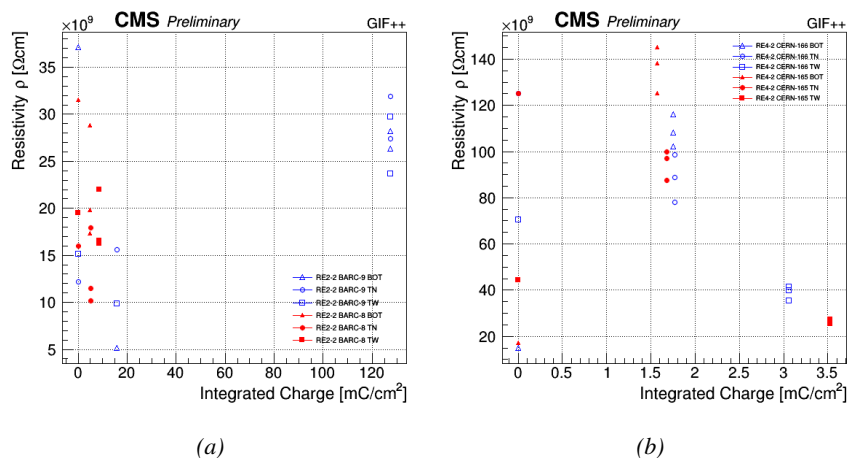


Figure 5.20: Evolution of the Bakelite resistivity for RE2 (5.20a) and RE4 (5.20b) detectors. Both irradiated (blue) and non irradiated (red) chambers are shown.

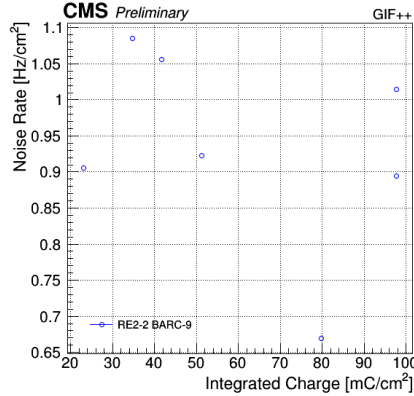


Figure 5.21: Evolution of the noise rate per unit area for the irradiated chamber RE2-2-BARC-9 only.

5.3.1 Description of the Data Acquisition

For the longevity studies, four spare chambers of the present system are used. Two spare RPCs of the RE2,3 stations as well as two spare RPCs from the new RE4 stations have been mounted in a Trolley. Six RE4 gaps are also placed in the trolley. The trolley is placed inside the GIF++ in the upstream region of the bunker, taking the cesium source as a reference. The trolley is oriented for the detection surface of the chambers to be orthogonal to the beam line. The system can be moved along the orthogonal plane in order to have the beam in all η -partitions. For the aging the trolley is moved outside the beam line and is placed in a distance of 5.2 m to the source, which irradiates the bunker using an attenuation filter of 2.2 which corresponds to a fluence of 10^7 gamma/cm².

During GIF++ operation, the data collected can be divided into different categories as several parameters are monitored in addition to the usual RPC performance data. On one hand, to know the performance of a chamber, it is need to measure its efficiency and to know the background conditions in which it is operated. To do this, the hit signals from the chamber are recorded and stored in a ROOT file via a Data Acquisition (DAQ) software. On the other hand, it is also very important to monitor parameters such as environmental pressure and temperature, gas temperature and humidity, RPC HV, LV, and currents, or even source and beam status. This is done through the GIF++ web Detector Control Software (DCS) that stores this information in a database.

Two different types of tests are conducted on RPCs via the DAQ. Indeed, the performance of the detectors is measured periodically during dedicated test beam periods using the H4 muon beam. In between these test beam periods, when the beam is not available, the chambers are irradiated by the ^{137}Cs in order to accu-

853 mulate deposited charge and the gamma background is measured.

854 RPCs under test are connected through LVDS cables to V1190A Time-to-
 855 Digital Converter (TDC) modules manufactured by CAEN. These modules, lo-
 856 cated in the rack area outside of the bunker, get the logic signals sent by the cham-
 857 bers and save them into their buffers. Due to the limited size of the buffers, the
 858 collected data is regularly erased and replaced. A trigger signal is needed for the
 859 TDC modules to send the useful data to the DAQ computer via a V1718 CAEN
 860 USB communication module.

861 In the case of performance test, the trigger signal used for data acquisition is
 862 generated by the coincidence of three scintillators. A first one is placed upstream
 863 outside of the bunker, a second one is placed downstream outside of the bunker,
 864 while a third one is placed in front of the trolley, close by the chambers. Every time
 865 a trigger is sent to the TDCs, i.e. every time a muon is detected, knowing the time
 866 delay in between the trigger and the RPC signals, signals located in the right time
 867 window are extracted from the buffers and saved for later analysis. Signals are
 868 taken in a time window of 400 ns centered on the muon peak (here we could show
 869 a time spectrum). On the other hand, in the case of background rate measurement,
 870 the trigger signal needs to be "random" not to measure muons but to look at gamma
 871 background. A trigger pulse is continuously generated at a rate of 300 Hz using a
 872 dual timer. To integrate an as great as possible time, all signals contained within
 873 a time window of 10us prior to the random trigger signal are extracted form the
 874 buffers and saved for further analysis (here another time spectrum to illustrate
 875 could be useful, maybe even place both spectrum together as a single Figure).

876 The signals sent to the TDCs correspond to hit collections in the RPCs. When a
 877 particle hits a RPC, it induce a signal in the pickup strips of the RPC readout. If this
 878 signal is higher than the detection threshold, a LVDS signal is sent to the TDCs.
 879 The data is then organised into 4 branches keeping track of the event number, the
 880 hit multiplicity for the whole setup, and the time and channel profile of the hits in
 881 the TDCs.

882 **5.3.2 RPC current, environmental and operation parameter mon- 883 itoring**

884 In order to take into account the variation of pressure and temperature between
 885 different data taking periods the applied voltage is corrected following the rela-
 886 tionship :

$$887 \quad HV_{eff} = HV_{app} \times \left(0.2 + 0.8 \cdot \frac{P_0}{P} \times \frac{T}{T_0} \right) \quad (5.10)$$

887 where T_0 (=293 K) and P_0 (=990 mbar) are the reference values.

888 5.3.3 Measurement procedure

- 889 Insert a short description of the online tools (DAQ, DCS, DQM).
- 890 Insert a short description of the offline tools : tracking and efficiency algorithm.
- 891 Identify long term aging effects we are monitoring the rates per strip.

892 5.3.4 Longevity studies results

6

893

894

Investigation on high rate RPCs

895 **6.1 Rate limitations and ageing of RPCs**

896 **6.1.1 Low resistivity electrodes**

897 **6.1.2 Low noise front-end electronics**

898 **6.2 Construction of prototypes**

899 **6.3 Results and discussions**

7

900

901

Conclusions and outlooks

902 **7.1 Conclusions**

903 **7.2 Outlooks**

References

904

- 905 [1] CERN. Geneva. LHC Experiments Committee. *The CMS muon project :
906 Technical Design Report*. Tech. rep. CERN-LHCC-97-032. CMS Collabora-
907 ration, 1997.
- 908 [2] CERN. Geneva. LHC Experiments Committee. *Technical Proposal for the
909 Phase-II Upgrade of the CMS Detector*. Tech. rep. CERN-LHCC-2015-010.
910 CMS Collaboration, 2015.
- 911 [3] CERN. Geneva. LHC Experiments Committee. *CMS, the Compact Muon
912 Solenoid : technical proposal*. Tech. rep. CERN-LHCC-94-38. CMS Col-
913 laboration, 1994.
- 914 [4] M. Abbrescia et al. “Study of long-term performance of CMS RPC under
915 irradiation at the CERN GIF”. In: *NIMA* 533 (2004), pp. 102–106.
- 916 [5] H.C. Kim et al. “Quantitative aging study with intense irradiation tests for
917 the CMS forward RPCs”. In: *NIMA* 602 (2009), pp. 771–774.
- 918 [6] S. Agosteo et al. “A facility for the test of large-area muon chambers at high
919 rates”. In: *NIMA* 452 (2000), pp. 94–104.
- 920 [7] PoS, ed. *CERN GIF ++ : A new irradiation facility to test large-area par-
921 ticle detectors for the high-luminosity LHC program*. Vol. TIPP2014. 2014,
922 pp. 102–109.
- 923 [8] M. Abbrescia et al. “Cosmic ray tests of double-gap resistive plate chambers
924 for the CMS experiment”. In: *NIMA* 550 (2005), pp. 116–126.
- 925 [9] A. Fagot. *GIF++ DAQ v4.0*. 2017. URL: https://github.com/afagot/GIF_DAQ.
- 927 [10] CAEN. *Mod. V1190-VX1190 A/B, 128/64 Ch Multihit TDC*. 14th ed. 2016.
- 928 [11] CAEN. *Mod. V1718 VME USB Bridge*. 9th ed. 2009.
- 929 [12] W-Ie-Ne-R. *VME 6021-23 VXI*. 5th ed. 2016.
- 930 [13] Wikipedia. *INI file*. 2017. URL: https://github.com/afagot/GIF_DAQ.
- 931

A

932

933 A data acquisition software for CAEN 934 VME TDCs

935 Certifying detectors in the perspective of HL-LHC required to develop tools for the
936 GIF++ experiment. Among them was the C++ Data Acquisition (DAQ) software
937 that allows to make the communications in between the computer and the TDC
938 modules in order to retrieve the RPC data [9]. In this appendix, details about the
939 software, as of how the software was written, how it functions and how it can be
940 exported to another similar setup.

941 **A.1 GIF++ DAQ file tree**

942 GIF++ DAQ source code is fully available on github at https://github.com/afagot/GIF_DAQ. The software requires 3 non-optional dependencies:

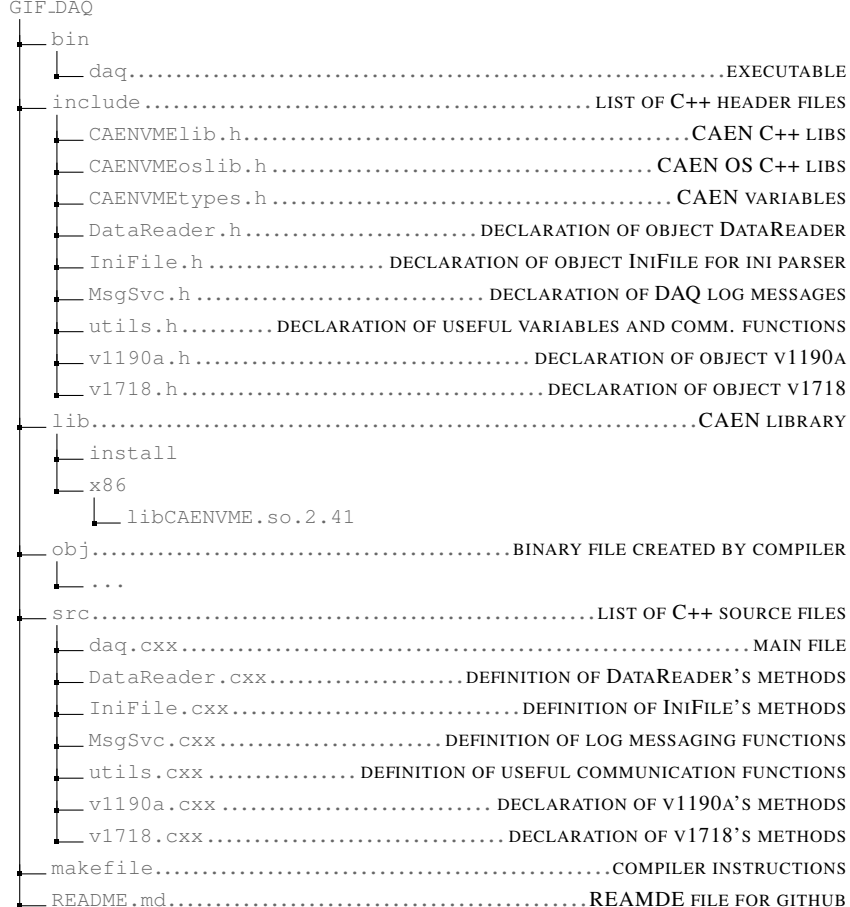
- 944 • CAEN USB Driver to mount the VME hardware
- 945 • CAEN VME Library to communicate with the VME hardware
- 946 • ROOT to organize the collected data into a TTree

947 The CAEN VME library will not be packaged by distributions and will need
948 to be installed manually. To compile the GIF++ DAQ project via a terminal, from
949 the DAQ folder use the command :

950 `make`

951 The source code tree is provided below along with comments to give an overview
 952 of the files' content. The different objects created for this project (v1718, v1190a,
 953 IniFile & DataReader) will be described in details in the following sections.

954



955 A.2 Description of the readout setup

956 The CMS RPC setup at GIF++ counts 5 V1190A Time-to-Digital Converter (TDC)
 957 manufactured by CAEN [10]. V1190A are VME units accepting 128 independent
 958 Multi-Hit/Multi-Event TDC channels whose signals are treated by 4 100 ps high
 959 performance TDC chips developped by CERN / ECP-MIC Division. The com-
 960 munication between the computer and the TDCs to transfer data is done via a
 961 V1718 VME master module also manufactured by CAEN and operated from a
 962 USB port [11]. These VME modules are all hosted into a 6U VME 6021 pow-

ered crate manufactured by W-Ie-Ne-R than can accomodate up to 21 VME bus cards [12]. These 3 components of the DAQ setup are shown in Figure A.1.

965

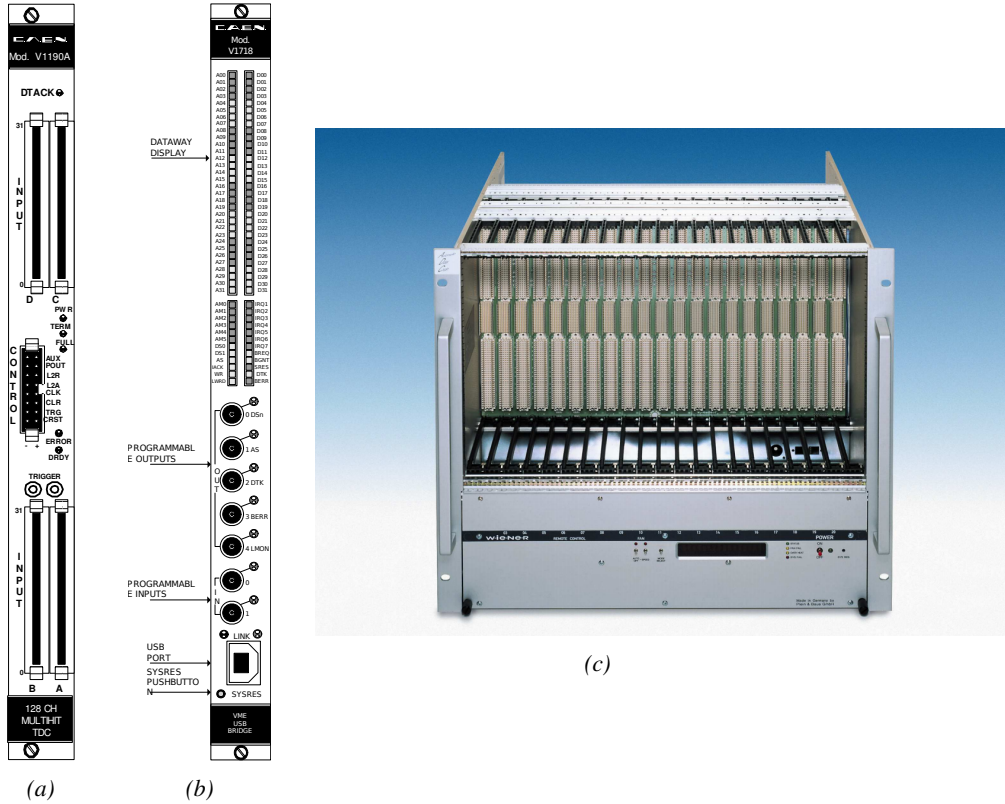


Figure A.1: (A.1a) View of the front panel of a V1190A TDC module [10]. (A.1b) View of the front panel of a V1718 Bridge module [11]. (A.1c) View of the front panel of a 6U 6021 VME crate [12].

A.3 Data read-out

To efficiently perform a data readout algorithm, C++ objects to handle the VME modules (TDCs and VME bridge) have been created along with objects to store data and read the configuration file that comes as an input of the DAQ software. It is useful to remind that the DAQ software in GIF++ is not a standalone software but is called through a Web Detector Control System (webDCS) application, that is the core of interactions with GIF++ setup, when data needs to be taken. Nevertheless, it is straight forward to make it into a standalone program that could be

966

967

968

969

970

971

972

973

974 adapted to any VME setup using V1190A and V1718 modules.

975

976 A.3.1 V1190A TDCs

977 The DAQ used at GIF takes profit of the *Trigger Matching Mode* offered by V1190A
 978 modules. This setting is enabled through the method `v1190a::SetTrigMatching`
 979 (`int ntdcs`) where `ntdcs` is the total number of TDCs in the setup this setting
 980 needs to be enabled for (Source Code A.1). A trigger matching is performed in
 981 between a trigger time tag, a trigger signal sent into the TRIGGER input of the
 982 TDC visible on Figure A.1a, and the channel time measurements, signals recorded
 983 from the detectors under test in our case. Control over this data acquisition mode,
 984 explained through Figure A.2, is offered via 4 programmable parameters:

- 985 • **match window:** the matching between a trigger and a hit is done within a
 986 programmable time window. This is set via the method

987 `void v1190a::SetTrigWindowWidth(UINT windowWidth, int ntdcs)`

- 988 • **window offset:** temporal distance between the trigger tag and the start of
 989 the trigger matching window. This is set via the method

990 `void v1190a::SetTrigWindowWidth(UINT windowWidth, int ntdcs)`

- 991 • **extra search margin:** an extended time window is used to ensure that all
 992 matching hits are found. This is set via the method

993 `void v1190a::SetTrigSearchMargin(UINT searchMargin, int ntdcs)`

- 994 • **reject margin:** older hits are automatically rejected to prevent buffer over-
 995 flows and to speed up the search time. This is set via the method

996 `void v1190a::SetTrigRejectionMargin(UINT rejectMargin, int ntdcs)`

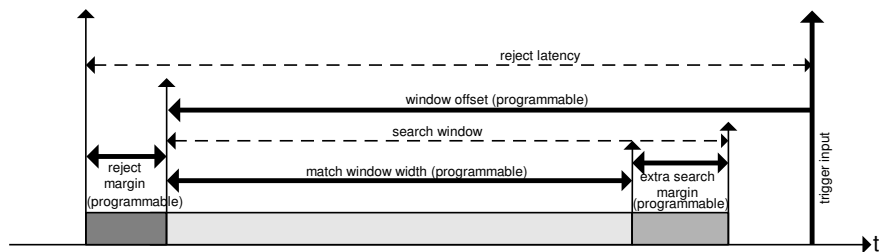


Figure A.2: Module V1190A Trigger Matching Mode timing diagram [10].

997 Each of these 4 parameters are given in number of clocks, 1 clock being 25 ns
 998 long. It is easy to understand at this level that there are 3 possible functioning
 999 settings:

- 1000 • **1:** the match window is entirely contained after the trigger signal,
- 1001 • **2:** the match window overlaps the trigger signal, or
- 1002 • **3:** the match window is entirely contained before the trigger signal as dis-
- 1003 played on Figure A.2.

1004 In both the first and second cases, the sum of the window width and of the
1005 offset can be set to a maximum of 40 clocks, which corresponds to 1 μ s. Evidently,
1006 the offset can be negative, allowing for a longer match window, with the constraint
1007 of having the window ending at most 1 μ s after the trigger signal. In the third case,
1008 the maximum negative offset allowed is of 2048 clocks (12 bit) corresponding to
1009 51.2 μ s, the match window being strictly smaller than the offset. In the case of
1010 GIF++, the choice has been made to use this last setting by delaying the trigger
1011 signal. During the studies performed in GIF++, both the efficiency of the RPCs,
1012 probed using a muon beam, and the noise or gamma background rate are moni-
1013 tored. The extra search and reject margins are left unused.

1014 To probe the efficiency of RPC detectors, the trigger time tag is provided by the
1015 coïncidence of scintillators when a bunch of muons passes through GIF++ area is
1016 used to trigger the data acquisition. For this measurement, it is useful to reduce the
1017 match window width only to contain the muon information. Indeed, the delay in
1018 between a trigger signal and the detection of the corresponding muon in the RPC
1019 being very contant (typically a few tens of ns due to jitter and cable length), the
1020 muon signals are very localised in time. Thus, due to a delay of approximalety
1021 325 ns in between the muons and the trigger, the settings where chosen to have a
1022 window width of 24 clocks (600 ns) centered on the muon peak thanks to a nega-
1023 tive offset of 29 clocks (725 ns).

1024 On the otherhand, monitoring the rates don't require for the DAQ to look at a
1025 specific time window. It is important to integrate enough time to have a robust
1026 measurement of the rate as the number of hits per time unit. The triggerring sig-
1027 nals is provided by a pulse generator at a frequency of 300 Hz to ensure that the
1028 data taking occurs in a random way, with respect to beam physics, to probe only
1029 the irradiation spectrum on the detectors. The match window is set to 400 clocks
1030 (10 μ s) and the negative offset to 401 clocks as it needs to exceed the value of the
1031 match window.

1032

1033 *Source Code A.1: Description of C++ object v1190a.*

```

class v1190a
{
    private :
        long             Handle;
        vector<Data32>   Address;
        CVDataWidth      DataWidth;
        CVAddressModifier AddressModifier;

    public:

        v1190a(long handle, IniFile *inifile, int ntdcs);
        ~v1190a();
        Data16 write_op_reg(Data32 address, int code, string error);
        Data16 read_op_reg(Data32 address, string error);
        void Reset(int ntdcs);
        void Clear(int ntdcs);
        void TestWR(Data16 value,int ntdcs);
        void CheckTDCStatus(int ntdcs);
        void CheckCommunication(int ntdcs);
        void SetTDCTestMode(Data16 mode,int ntdcs);
        void SetTrigMatching(int ntdcs);
        void SetTrigTimeSubtraction(Data16 mode,int ntdcs);
        void SetTrigWindowWidth(Uint windowHeight,int ntdcs);
        void SetTrigWindowOffset(Uint windowOffset,int ntdcs);
        void SetTrigSearchMargin(Uint searchMargin,int ntdcs);
        void SetTrigRejectionMargin(Uint rejectMargin,int ntdcs);
        void GetTrigConfiguration(int ntdcs);
        void SetTrigConfiguration(IniFile *inifile,int ntdcs);
        void SetTDCDetectionMode(Data16 mode,int ntdcs);
        void SetTDCResolution(Data16 lsb,int ntdcs);
        void SetTDCDeadTime(Data16 time,int ntdcs);
        void SetTDCHeadTrailer(Data16 mode,int ntdcs);
        void SetTDCEventSize(Data16 size,int ntdcs);
        void SwitchChannels(IniFile *inifile,int ntdcs);
        void SetIRQ(Data32 level, Data32 count,int ntdcs);
        void SetBlockTransferMode(Data16 mode,int ntdcs);
        void Set(IniFile *inifile,int ntdcs);
        void CheckStatus(CVErrorCodes status) const;
        int ReadBlockD32(Uint tdc, const Data16 address,
                         Data32 *data, const Uint words, bool ignore_berr);
        Uint Read(RAWData *DataList,int ntdcs);
    };

```

1035 The v1190a object, defined in the DAQ software as in Source Code A.1, offers
1036 the possibility to concatenate all TDCs in the readout setup into a single object con-
1037 taining a list of hardware addresses (addresses to access the TDCs' buffer through
1038 the VME crate) and each constructor and method acts on the list of TDCs.
1039

1040 A.3.2 DataReader

1041 Enabled thanks to v1190a::SetBlockTransferMode(Data16 mode, int ntdcs),
1042 the data transfer is done via Block Transfer (BLT). Using BLT allows to tranfer a
1043 fixed number of events called a *block*. This is used together with an Almost Full

1044 Level (AFL) of the TDCs' output buffers, defined through `v1190a::SetIRQ(Data32`
1045 `level, Data32 count, int ntdcs)`. This AFL gives the maximum amount of
1046 32735 words (16 bits, corresponding to the depth of a TDC output buffer) that
1047 can written in a buffer before an Interrupt Request (IRQ) is generated and seen by
1048 the VME Bridge, stopping the data acquisition to transfer the content of each TDC
1049 buffers before resuming. For each trigger, 6 words or more are written into the
1050 TDC buffer:

- 1051 • a **global header** providing information of the event number since the begin-
1052 ning of the data acquisition,
- 1053 • a **TDC header**,
- 1054 • the **TDC data** (*if any*), 1 for each hit recorded during the event, providing
1055 the channel and the time stamp associated to the hit,
- 1056 • a **TDC error** providing error flags,
- 1057 • a **TDC trailer**,
- 1058 • a **global trigger time tag** that provides the absolute trigger time relatively
1059 to the last reset, and
- 1060 • a **global trailer** providing the total word count in the event.

1061 As previously described in Section 4.4.3, CMS RPC FEEs provide us with
1062 100 ns long LVDS output signals that are injected into the TDCs' input. Any
1063 avalanche signal that gives a signal above the FEEs threshold is thus recorded by
1064 the TDCs as a hit within the match window. Each hit is assigned to a specific TDC
1065 channel with a time stamp, with a precision of 100 ps. The reference time, $t_0 = 0$,
1066 is provided by the beginning of the match window. Thus for each trigger, coming
1067 from a scintillator coïncidence or the pulse generator, a list of hits is stored into
1068 the TDCs' buffers and will then be transferred into a ROOT Tree.

1069
1070 When the BLT is used, it is easy to understand that the maximum number of
1071 words that have been set as ALF will not be a finite number of events or, at least,
1072 the number of events that would be recorded into the TDC buffers will not be a
1073 multiple of the block size. In the last BLT cycle to transfer data, the number of
1074 events to transfer will most probably be lower than the block size. In that case, the
1075 TDC can add fillers at the end of the block but this option requires to send more
1076 data to the computer and is thus a little slower. Another solution is to finish the
1077 transfer after the last event by sending a bus error that states that the BLT reached
1078 the last event in the pile. This method has been chosen in GIF++.

1079

1080 Due to irradiation, an event in GIF++ can count up to 300 words per TDC. A
 1081 limit of 4096 words (12 bits) has been set to generate IRQ which represent from
 1082 14 to almost 700 events depending on the average of hits collected per event. Then
 1083 the block size has been set to 100 events with enabled bus errors. When an AFL
 1084 is reached for one of the TDCs, the VME bridge stops the acquisition by sending
 1085 a BUSY signal.

1086

1087 The data is then transferred one TDC at a time into a structure called `RAWData`
 1088 (Source Code A.2).

1089

1090 *Source Code A.2: Description of data holding C++ structure `RAWData`.*

```
1091     struct RAWData{
1092         vector<int>                     *EventList;
1093         vector<int>                     *NHitsList;
1094         vector<int>                     *QFlagList;
1095         vector<vector<int> >     *ChannelList;
1096         vector<vector<float> >    *TimeStampList;
1097     };
```

1092 In order to organize the data transfer and the data storage, an object called
 1093 `DataReader` was created (Source Code A.3). On one hand, it has `v1718` and `v1190a`
 1094 objects as private members for communication purposes, such as VME modules
 1095 settings via the configuration file `*iniFile` or data read-out through `v1190a::Read()`
 1096 and on the other hand, it contains the structure `RAWData` that allows to organise the
 1097 data in vectors reproducing the tree structure of a ROOT file.

1098

1099 *Source Code A.3: Description of C++ object `DataReader`.*

```

class DataReader
{
    private:
        bool      StopFlag;
        IniFile *iniFile;
        Data32   MaxTriggers;
        v1718    *VME;
        int       nTDCs;
        v1190a   *TDCs;
        RAWData  TDCData;

    public:
        DataReader();
        virtual ~DataReader();
        void     SetIniFile(string inifilename);
        void     SetMaxTriggers();
        Data32   GetMaxTriggers();
        void     SetVME();
        void     SetTDC();
        int      GetQFlag(Uint it);
        void     Init(string inifilename);
        void     FlushBuffer();
        void     Update();
        string   GetFileName();
        void     WriteRunRegistry(string filename);
        void     Run();
};

1101   Each event is transferred from TDCData and saved into branches of a ROOT
1102   TTree as 3 integers that represent the event ID (EventCount), the number of hits
1103   read from the TDCs (nHits), and the quality flag that provides information for any
1104   problem in the data transfer (qflag), and 2 lists of nHits elements containing the
1105   fired TDC channels (TDCh) and their respective time stamps (TDCTS), as presented
1106   in Source Code A.4. An example of ROOT data file is provided with Figure A.3.
1107

```

*Source Code A.4: Highlight of the data transfer and organisation within
`DataReader::Run()` after the data has been collected into `TDCData`.*

```
RAWData TDCData;
TFile *outputFile = new TFile(outputFileName.c_str(), "recreate");
TTree *RAWDataTree = new TTree("RAWData", "RAWData");

int EventCount = -9;
int nHits = -8;
int qflag = -7;
vector<int> TDCCh;
vector<float> TDCTS;

RAWDataTree->Branch("EventNumber", &EventCount, "EventNumber/I");
RAWDataTree->Branch("number_of_hits", &nHits, "number_of_hits/I");
RAWDataTree->Branch("Quality_flag", &qflag, "Quality_flag/I");
RAWDataTree->Branch("TDC_channel", &TDCCh);
RAWDataTree->Branch("TDC_TimeStamp", &TDCTS);

for(UInt i=0; i<TDCData.EventList->size(); i++) {
    EventCount = TDCData.EventList->at(i);
    nHits = TDCData.NHitsList->at(i);
    qflag = TDCData.QFlagList->at(i);
    TDCCh = TDCData.ChannelList->at(i);
    TDCTS = TDCData.TimeStampList->at(i);
    RAWDataTree->Fill();
}

//...
//Here read the TDC data using v1190a::Read() and place it into
//TDCData for as long as you didn't collect the requested amount
//of data.
//...
```

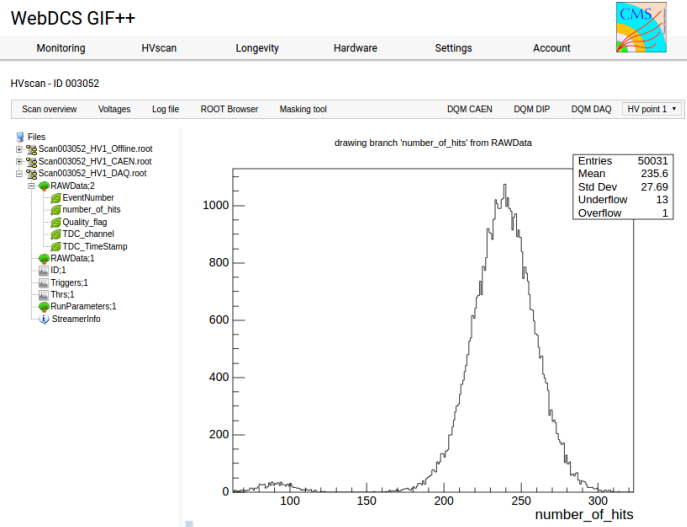


Figure A.3: Structure of the ROOT output file generated by the DAQ. The 5 branches (EventNumber, number_of_hits, Quality_flag, TDC_channel and TDC_TimeStamp) are visible on the left panel of the ROOT browser. On the right panel is visible the histogram corresponding to the variable nhits. In this specific example, there were approximately 50k events recorded to measure the gamma irradiation rate on the detectors. Each event is stored as a single entry in the TTree.

1110 A.4 Communications

1111 To ensure data readout and dialog in between the machine and the TDCs or in
 1112 between the webDCS and the DAQ, different communication solutions were used.
 1113 First of all, it is important to have a module to allow the communication in between
 1114 the TDCs and the computer from which the DAQ operates. When this communica-
 1115 tion is effective, shifters using the webDCS to control data taking can thus send
 1116 instructions to the DAQ.

1117

1118 A.4.1 V1718 USB Bridge

1119 In the previous section, the data transfer has been discussed. The importance of
 1120 the v1718 object (Source Code A.5), used as private member of DataReader,
 1121 was not explicated. VME master modules are used for communication purposes
 1122 as they host the USB port that connects the powered crate buffer to the com-
 1123 puter where the DAQ is installed. From the source code point of view, this ob-
 1124 ject is used to control the communication status, by reading the returned error
 1125 codes with v1718::CheckStatus(), or to check for IRQs coming from the TDCs

1126 through `v1718::CheckIRQ()`. Finally, to ensure that triggers are blocked at the
 1127 hardware level, a NIM pulse is sent out of one of the 5 programmable outputs
 1128 (`v1718::SendBUSY()`) to the VETO of the coincidence module where the trigger
 1129 signals originate from. As long as this signal is ON, no trigger can reach the TDCs
 1130 anymore.

1131

1132 *Source Code A.5: Description of C++ object v1718.*

```
1133
class v1718{
    private:
        int Handle;
        Data32 Data;           // Data
        CVIRQLevels Level;     // Interrupt level
        CVAddressModifier AM;   // Addressing Mode
        CVDataWidth dataSize;  // Data Format
        Data32 BaseAddress;    // Base Address

    public:
        v1718(IniFile *iniFile);
        ~v1718();
        long GetHandle(void) const;
        int SetData(Data16 data);
        Data16 GetData(void);
        int SetLevel(CVIRQLevels level);
        CVIRQLevels GetLevel(void);
        int SetAM(CVAddressModifier am);
        CVAddressModifier GetAM(void);
        int SetDatasize(CVDataWidth dataSize);
        CVDataWidth GetDataSize(void);
        int SetBaseAddress(Data16 baseaddress);
        Data16 GetBaseAddress(void);
        void CheckStatus(CVErrorCodes status) const;
        void CheckIRQ();
        void SetPulsers();
        void SendBUSY(BusyLevel level);
};
```

1134 **A.4.2 Configuration file**

1135 The DAQ software takes as input a configuration file written using INI standard [13].
 1136 This file is partly filled with the information provided by the shifters when starting
 1137 data acquisition using the webDCS, as shown by Figure A.4. This information is
 1138 written in section `[General]` and will later be stored in the ROOT file that con-
 1139 tains the DAQ data as can be seen from Figure A.3. Indeed, another `TTree` called
 1140 `RunParameters` as well as the 2 histograms `ID`, containing the scan number, start
 1141 and stop time stamps, and `Triggers`, containing the number of triggers requested
 1142 by the shifter, are available in the data files.

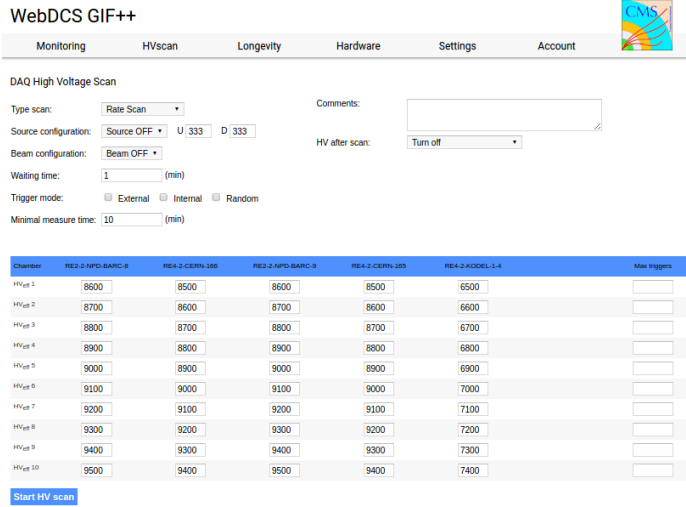


Figure A.4: WebDCS DAQ scan page. On this page, shifters need to choose the type of scan (Rate, Efficiency or Noise Reference scan), the gamma source configuration at the moment of data taking, the beam configuration, and the trigger mode. These information will be stored in the DAQ ROOT output. Are also given the minimal measurement time and waiting time after ramping up of the detectors is over before starting the data acquisition. Then, the list of HV points to scan and the number of triggers for each run of the scan are given in the table underneath.

1143 The rest of the information is written beforehand in the configuration file template,
 1144 as explicited in Source Code A.6, and contains the hardware addresses to
 1145 the differentes VME modules in the setup as well as settings for the TDCs. As the
 1146 TDC settings available in the configuration file are not supposed to be modified, an
 1147 improvement would be to remove them from the configuration file and to hardcode
 1148 them inside of the DAQ code itself or to place them into a different INI file that
 1149 would host only the TDC settings to lower the probability for a bad manipulation
 1150 of the configuration file that can be modified from one of webDCS' menus.

1151

Source Code A.6: INI configuration file template for 4 TDCs. In section [**General1**], the number of TDCs is explicited and information about the ongoing run is given. Then, there are sections for each and every VME modules. There buffer addresses are given and for the TDCs, the list of channels to enable is given. Finally, in section [**TDCSettings**], a part of the TDC settings are given.
 1152

```

[General]
TdcS=4
ScanID=$scanid
HV=$HV
RunType=$runtype
MaxTriggers=$maxtriggers
Beam=$beam
[VMEInterface]
Type=V1718
BaseAddress=0xF0000
Name=VmeInterface
[TDC0]
Type=V1190A
BaseAddress=0x00000000
Name=Tdc0
StatusA0-15=1
StatusA16-31=1
StatusB00-15=1
StatusB16-31=1
StatusC00-15=1
StatusC16-31=1
StatusD00-15=1
StatusD16-31=1
[TDC1]
Type=V1190A
BaseAddress=0x11110000
Name=Tdc1
StatusA0-15=1
StatusA16-31=1
StatusB00-15=1
StatusB16-31=1
StatusC00-15=1
StatusC16-31=1
StatusD00-15=1
StatusD16-31=1
1153 [TDC2]
Type=V1190A
BaseAddress=0x22220000
Name=Tdc2
StatusA0-15=1
StatusA16-31=1
StatusB00-15=1
StatusB16-31=1
StatusC00-15=1
StatusC16-31=1
StatusD00-15=1
StatusD16-31=1
[TDC3]
Type=V1190A
BaseAddress=0x44440000
Name=Tdc3
StatusA0-15=1
StatusA16-31=1
StatusB00-15=1
StatusB16-31=1
StatusC00-15=1
StatusC16-31=1
StatusD00-15=1
StatusD16-31=1
[TDCSettings]
TriggerExtraSearchMargin=0
TriggerRejectMargin=0
TriggerTimeSubtraction=0b1
TdcDetectionMode=0b01
TdcResolution=0b10
TdcDeadTime=0b00
TdcHeadTrailer=0b1
TdcEventSize=0b1001
TdcTestMode=0b0
BLTMode=1

```

1154 A.4.3 WebDCS/DAQ intercommunication

1155 When shifters send instructions to the DAQ via the configuration file, it is the web-
 1156 DCS itself that gives the start command to the DAQ and then the 2 softwares use
 1157 inter-process communication through file to synchronise themselves. This com-
 1158 munication file is represented by the variable `const string __runstatuspath`.
 1159 On one side, the webDCS sends commands or status that are readout by the DAQ:

- 1160 • INIT, status sent when launching a scan and read via function `CtrlRunStatus(...)`,

- 1161 • START, command to start data taking and read via function `CheckSTART()`,
- 1162 • STOP, command to stop data taking at the end of the scan and read via
1163 function `CheckSTOP()`, and
- 1164 • KILL, command to kill data taking sent by user and read via function `CheckKILL()`

1165 and on the other, the DAQ sends status that are controled by the webDCS:

- 1166 • DAQ_RDY, sent with `SendDAQReady()` to signify that the DAQ is ready to
1167 receive commands from the webDCS,
- 1168 • RUNNING, sent with `SendDAQRunning()` to signify that the DAQ is taking
1169 data,
- 1170 • DAQ_ERR, sent with `SendDAQError()` to signify that the DAQ didn't receive
1171 the expected command from the webDCS or that the launch command didn't
1172 have the right number of arguments,
- 1173 • RD_ERR, sent when the DAQ wasn't able to read the communication file,
1174 and
- 1175 • WR_ERR, sent when the DAQ wasn't able to write into the communication
1176 file.

1177 A.4.4 Example of inter-process communication cycle

1178 Under normal conditions, the webDCS and the DAQ processes exchange com-
1179 mands and status via the file hosted at the address `__runstatuspath`, as explained
1180 in subsection A.4.3. An example of cycle is given in Table A.1. In this example,
1181 the steps 3 to 5 are repeated as long as the webDCS tells the DAQ to take data.
1182 A data taking cycle is the equivalent as what is called a *Scan* in GIF++ jargon,
1183 referring to a set a runs with several HV steps. Each repetition of steps 3 to 5 is
1184 then equivalent to a single *Run*.

1185
1186 At any moment during the data taking, for any reason, the shifter can decide
1187 that the data taking needs to be stopped before it reached the end of the scheduled
1188 cycle. Thus at any moment on the cycle, the content of the inter-process commu-
1189 nication file will be changed to KILL and the DAQ will shut down right away. The
1190 DAQ checks for KILL signals every 5s after the TDCs configuration is over. So
1191 far, the function `CheckKILL()` has been used only inside of the data taking loop
1192 of method `DataReader::Run()` and thus, if the shifter decides to KILL the data
1193 taking during the TDC configuration phase or the HV ramping in between 2 HV
1194 steps, the DAQ will not be stopped smoothly and a *force kill* command will be sent
1195 to stop the DAQ process that is still awake on the computer. Improvements can be

step	actions of webDCS	status of DAQ	__runstatuspath
1	launch DAQ ramp voltages ramping over wait for currents stabilization	readout of IniFile configuration of TDCs	INIT
2		configuration done send DAQ ready wait for START signal	DAQ_RDY
3	waiting time over send START		START
4	wait for run to end monitor DAQ run status	data taking ongoing check for KILL signal	RUNNING
5		run over send DAQ_RDY wait for next DCS signal	DAQ_RDY
6	ramp voltages ramping over wait for currents stabilization		DAQ_RDY
3	waiting time over send START		START
4	wait for run to end monitor DAQ run status	update IniFile information data taking ongoing check for KILL signal	RUNNING
5		run over send DAQ_RDY wait for next DCS signal	DAQ_RDY
7	send command STOP	DAQ shuts down	STOP

Table A.1: Inter-process communication cycles in between the webDCS and the DAQ through file string signals.

¹¹⁹⁶ brought on this part of the software to make sure that the DAQ can safely shutdown
¹¹⁹⁷ at any moment.

¹¹⁹⁸

¹¹⁹⁹ **A.5 DAQ algorithm overview**

¹²⁰⁰ **A.6 Software export**

B

1201

1202 Details on the online analysis package

1203 **B.1 Introduction**

1204 insert text here

C

1205

1206

1207

Structure of the hybrid simulation software

1208 C.1 Introduction

1209 insert text here...

